Title
Nuclear Magnetic Resonance Study of Crystalline Polarized Rotors, and Strontium Ruthenate

Author
Su, Yue-Shun

Publication Date
2020

Peer reviewed|Thesis/dissertation

UNIVERSITY OF CALIFORNIA

Los Angeles

Nuclear Magnetic Resonance Study of Crystalline Polarized Rotors, and Strontium Ruthenate

A dissertation submitted in partial satisfaction

of the requirements for the degree

Doctor of Philosophy in Materials Science and Engineering

by

Yue-Shun Su

2020

ABSTRACT OF THE DISSERTATION

Nuclear Magnetic Resonance Study of Crystalline Polarized Rotors, and Strontium Ruthenate

by

Yue-Shun Su
Doctor of Philosophy in Materials Science and Engineering
University of California, Los Angeles, 2020
Professor Bruce Dunn, Co-chair
Professor Stuart Brown, Co-chair

The design of molecular machines will depend on incorporating functionalized degrees of freedom into the final product. Toward that end, we examine the physical properties of a crystalline system containing a nearly free rotator synthesized to include an electric dipole moment. Crystals of reorienting 2,2-difluoro-1,4-bicyclo[2.2.2]octane-dicarboxylate (F_2-BODCA) acting as linker and rotator in a metal organic framework (MOF) with Zn(II)-nodes and 1,4-diaza-bicyclo[2.2.2]octane (dabco) spacers, revealed emergent order as a result of dipole-dipole interactions. Variable temperature, frequency-dependent dielectric measurements consisting of a relatively sharp maximum in capacitance at $T_c = 100$ K was observed when a rapidly rotating, dipole-disordered, paraelectric phase, transformed into an ordered, antiferroelectric phase. A frequency-dependent Debye-like dynamic crossover was detected when the rotor dynamics become slower than the frequency of the alternating electric field. The dynamic nature of the F_2-BODCA rotators was confirmed by NMR spectroscopy, and the energetics of the rotational profile elucidated with the help of Density Functional Theory (DFT) calculations. Finally, Monte Carlo simulations on a 2D rotary lattice revealed a ground state with an Ising symmetry and the effects of dipole-lattice and dipole-dipole interactions.

In a second project, magnetic resonance methods were used to study the superconductivity of Sr_2RuO_4. Over the past 20 years, the superconducting state of Sr_2RuO_4, a material that is quasi-two-dimensional perovskite and strongly correlated, was considered to be the only solid-state analogue to the superfluid ^{3}He-A phase [1, 2], with an odd-parity order parameter that is unidirectional in spin space for all electron momenta and breaks time-reversal symmetry. A consequence is the expectation of a 'split' transition in a Sr_2RuO_4 crystal with the presence of in-plane uniaxial strain. Such behavior has not yet been observed in thermodynamic measurements. Instead, on increasing the uniaxial compressive stress, a peak in transition temperature was observed [3, 4]. In this work, we utilised oxygen-17 solid state nuclear magnetic resonance spectroscopy to probe the electron spin degrees of freedom via the hyperfine interaction as a means of constraining the possible order parameter symmetry. Reduction of the Knight shift is observed for all strains at temperatures below the critical temperature, corresponding well to the drop in spin polarization. The result contradicts prior NMR results [5], and excludes the previously favored topological superconducting state.

The dissertation of Yue-Shun Su is approved.

Kang Lung Wang

Xiaochun Li

Bruce Dunn, Committee Co-chair

Stuart Brown, Committee Co-chair

University of California, Los Angeles

2020

To my mother ...

who gives me unconditional love

To my father ...

who holds me on his shoulders

To uncertainty ...

which perturbs me to another state

extemporaneously

Table of Contents

List of Figures

Acknowledgements

First and foremost, I am indebted to my advisor Dr. Stuart Brown. Thank you very much for taking me on board to your condensed matter physics NMR lab notwithstanding my materials science background. It is a rare and valuable experience. You provided me with the precious opportunities of learning to approach problems from a physicist's point of view, and demonstrated what a top-notch scientist should be like. For instance, how to plan experiments, to build apparatus, to evaluate the relationship between physical parameters, and to think meticulously and to justify firmly, both qualitatively and quantitatively. I am grateful for your cultivating me through interrogation. I am sure there are unknown muscles grown since it was not as smooth and easy, and I thank those machines and gadgets I fixed, and the rotor paper with your guidance. The countless iteration trains my ability to write and inform a concerted story, while paying attention to macroscopic structure and microscopic details. If you recalled, at the end of my oral defense, the three professors on the committee congratulated you by saying "Stuart, you did a good job", then I know I did not let you down. In particular, my sincere gratitude is expressed to Dr. Bruce Dunn, Dr. Kang Wang, and Dr. Xiaochun Li for kindly spending your time and lending the helping hands to serve on my committee. I hope this thesis writing worth your time reading and I look forward to your kind suggestions.

To my colleagues, it is my privilege to work with you and learn from you. Georgios and Hank provided kind introduction and guidance to NMR. Hank played volleyball together, and lent me your hair-cutter and your car. Thanks Yongkang, as a mentor, for deepening my understanding and accumulated my sense of doing hands-on experiment, Andrej, being agile and tactful, demonstrated how crucially essential articulation is in the academic regime, Pedro for always being the reliable person to go to and playing basketball together, Erik for spearheading the dielectric measurement and initiating Monte Carlo simulation, Aaron for working with ^2H NMR measurement and with Andrew, who has fairly competent programming skills, on Monte Carlo simulation. Thanks Ieva for the beautiful density function

theory calculation. Thanks Anisha and Isabella for the chances to work and learn together for your projects. Alvin, Teresa, thanks for the dialogues that enhanced my understanding regarding American culture.

To my fellow University Cooperation Housing Association friends, while the existence of yours seems commonplace from a day-to-day viewpoint, it is of crucial importance as a strong supportive peer group. Albeit you came and went non-stop as flowing water without time reversal symmetry (TRS)[1], I hope all of us are doing well when facing local minimums and maximums in the navigation of our lives, and do not cease subliming ourselves. I am grateful for us constituting the home away from home.

To my dear family. Thank you for supporting me all the way through, although you do not agree with my decision of studying abroad at all. I know it is too far away from home and you feel unsettled because I am exposed to so many uncertainties that you never experienced. But it is how I can grow, and you know my heart is always around and accompanying. My childhood diary you dig out earlier featuring "...there are 8 members in my family..." gives me strength to carry on. To my beloved wife, you have been enhancing me in many aspects to a large extent. Thank you for being my role model and by my side. It is often quoted that a good couple mutually improves one another, and I think you and I are manifesting it together. You are always there considerately and thoughtfully listening to my frustration and sharing my stress as well as happiness. The journey has been and will continue to be colorful and cannot be fulfilled without your warm company and gourmet negative entropy.

[1]Notwithstanding being a statistical emergence that is supposed to be related to entropy, the reason why statistics beats TRS is evasive to me.

Curriculum Vitae

2006 – 2010	B.S. Materials Science and Engineering, National Tsing Hua University (NTHU), Double Specialty Program
2010 – 2013	M.S. Materials Science and Engineering, NTHU
2014 – 2020	Graduate Researcher, Materials Science and Engineering, University of California, Los Angeles (UCLA)

Publications

[1] Y.-S. Su, E. Lamb, I. Liepuoniute, A. Chronister, A. Stanton, P. Guzman, S. Perez-Estrada, T. Chang, K. N. Houk, M. Garcia-Garibay, and S. E. Brown, "Emergent dipolar order in amphidynamic crystals with reorienting polar linkers," Nature Chemistry, accepted .

[2] A. Pustogow, Y. Luo, A. Chronister, Y.-S. Su, D. A. Sokolov, F. Jerzembeck, A. P. Mackenzie, C. W. Hicks, N. Kikugawa, S. Raghu, E. D. Bauer, and S. E. Brown, "Constraints on the superconducting order parameter in Sr_2RuO_4 from oxygen-17 nuclear magnetic resonance," Nature **574**, 72-75(2019), arXiv:1904.00047 [hep-ph]

CHAPTER 1

Introduction

1.1 Introduction to Rotor Project

During a talk in 1984, Richard Feynman said to the audience: "Now let us talk about the possibility of making machines with movable parts, which are very tiny." Inspired by the nano machines already existing in nature, such as bacterial flagella which are spinning molecules rendering a bacteria move forward, bio-energy to mechanical energy, he advocated the possibility of nanotechnology for building artificial nano functional machines and envisioned it would be realized in the future. Many researchers were then inspired by the idea and made efforts to create functional molecular complexes [9].

The building blocks of a molecular complex should be able to move relative to each other, so as to serve as a functional molecular machine. For instance, in 1983 Jean-Pierre Sauvage's group at CNRS, France, managed to assemble a chain with two rings interlocked, one being responsive to energy input and is capable of revolving around the other ring in a regulated fashion. The phenomenon that one part of the assembly can be well-regulated due to external stimuli heralds the future of controllable molecular machines. In addition, Fraser Stoddart's group at UCLA additionally demonstrated an elevator toy model that can uplift itself by 0.7 nanometers from a reference surface [9, 10], and can be moved reversibly by changing the acid and basic environment of the solution.

1.1.1 Features of Molecular Machines

Molecular machines encompass special characteristics. Compared to macroscopic machines which are influenced by friction and inertial forces, molecular machines are affected by thermal fluctuation and the hindrance to motion exerted by their surroundings. The interaction of a molecular complex with its surrounding could be described by a potential energy surface, which could include steric interaction[1]. After individual components are assembled into a molecular functional complex, the total number of degrees of freedom is largely decreased, namely total entropy is reduced. Similar to macroscopic machines, molecular machines should have multi components, one of which is responsive to external perturbation. Moreover, with adequate thermal energy, for instance at ambient temperature, molecular machines would not be motionless as compared to macroscopic machines. Consequently, due to thermal fluctuations, the motion of molecular machines is typically described as Brownian [2]. For another aspect, the nature of the potential landscape is contingent on the details of interactions, and structural variation of the molecules [6, 11, 12].

1.1.2 Crystalline Molecular Rotors

Molecular machines offer a rich platform for the study of physics. With the ultimate goal of devising controllable molecular machines, scientists have been stretching their imagination and implementing feasible ideas on the nanoscale. Condensed matter materials system bearing anisotropic molecular ordering and correlated dynamics is a fairly decent candidate to be focused on, since it has the potential to realize the aspiration of molecular machines with controllable properties[3]. A promising is crystalline molecular rotors [13–16], since it not only provides stable and rigid crystalline framework, but also imparts enough space for

[1]Steric interaction is the manifestation of Pauli exclusion principle, dictating that electron clouds keep a distance from one another.

[2]A caveat: the constraints of the motions of the molecules could lead to deviation from Brownian.

[3]Ferrolelectric correlation is especially favored since it can be readily manipulated by applying electric fields.

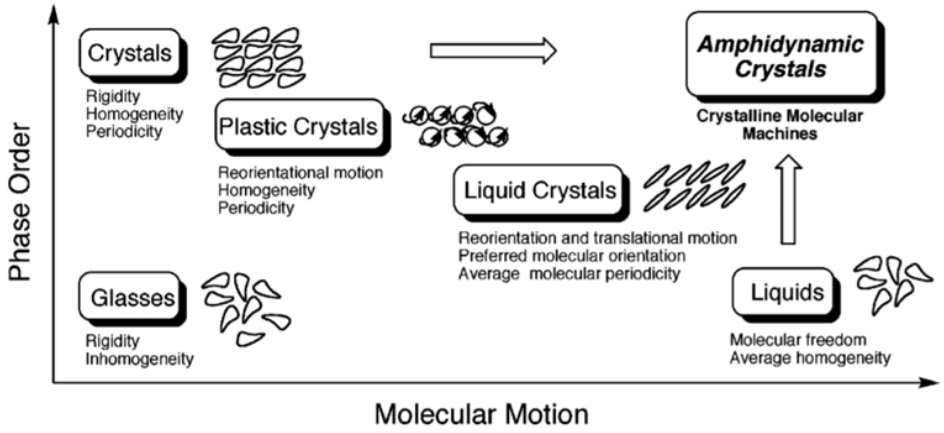

Figure 1.1: Conceptual map constituted by dynamic degree of freedom and the extent of crystallinity. Typically in condensed matter materials, there is a trade-off between dynamics and crystallinity. The artificially designed amphidynamic crystal can circumvent the trade-off and is situated at the upper right part of the map, with its framework maintaining high ordering and sufficient space, which allows for molecular motion at the same time [6].

rotational degrees of freedom. This category of materials is coined amphidynamic, bearing both crystallinity and motional degrees of freedom, as shown in Fig. 1.1. The framework is made up of two triptycyl groups to ensure the free volume between them [6, 17]. If the rotating molecules are equipped with electric dipole moments by attaching atoms with high electron negativity such as fluorines, correlated phenomenon could be derived depending on the dipolar interaction among the rotors in the crystal.

1.1.3 Objective of the Rotor Research

The long term objective of this work is to utilize the crystalline molecular rotors to realize functionality. Nonetheless, we are in the incipient exploratory phase where the efforts made are to experiment with how different parameters of crystalline molecular rotors can influence the thermodynamics and dynamics of the rotating molecules. For dipolar crystalline molecular rotors, variables include crystal structure, the free space it provides, flexibility of the framework, the symmetry, size, and spatial configuration of the rotating dipolar molecules,

the distance between adjacent rotating dipolar molecules, and the strength of the individual permanent electric dipole moments, among others. We will then hope to accumulate more knowledge, so as to design rotors that behave as we desire for practical applications, controllable rotation at room temperature for instance.

1.1.4 NMR on Crystalline Molecular Rotors

In contrast to the dynamic processes on the macroscopic scale, which are as a function of moment of inertia and friction, dynamic processes on the molecular scale are highly contingent on thermal energy since the mass of each rotator is sufficiently small that thermal motion reorients the rotators. The interaction of rotors with its surrounding framework informs the rotation barrier. For instance, when the packing coefficient of the material is close to that of close-packing ca. 0.73, meaning the rotator is almost in contact with its surrounding framework, rotation is primarily affected by steric interaction. In this circumstance, the flexibility of the surrounding frameworks to give way to the rotating rotor is essential and therefore would determine the resultant dynamics. If the surrounding frameworks can move according to the rotating molecule in a concerted fashion, the overall hindrance to the rotation is reduced. On the other hand, if the packing coefficient is decreased and more available space for rotation, the limitation to rotation is relieved [18–20].

Since thermal energy serves as the driving force for the rotation, Arrhenius thermal activated behavior is typically assumed to delineate the Brownian motion,

$$\omega_{rot} = \omega_0 \ exp(-\frac{E_a}{k_B T}), \tag{1.1}$$

where the E_a is activation energy, quantifying the resultant hindrance, for each molecule to rotate from one equilibrium position to the adjacents classically. k_BT is the thermal energy. The pre-factor ω_0, also named the attempt-to-escape frequency, is determined, in part, by the moment of inertia of the rotator. With higher thermal energy input, the molecules in the sample are more likely to jump to an adjacent position [21–23], following the Boltzmann distribution. Fig. 1.2 exemplifies how the rotation of a molecule in a condensed matter can

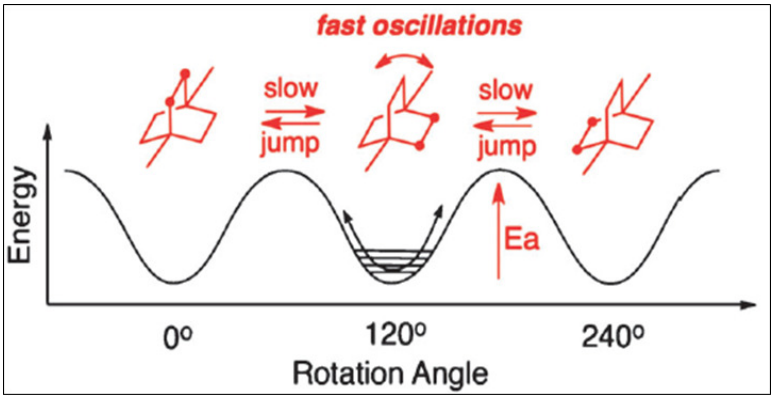

Figure 1.2: A rotational energy landscape with 3-fold symmetry. Rotor would jump from one lowest energy angle to another, with the probability contingent on the magnitude of activation energy E_a and the temperature of the thermal bath [6]. The symmetry of the rotational barrier is predicated on the symmetry of the rotator and the symmetry of the environment. For instance, if a 3-fold symmetric rotator is situated in a 2-fold symmetric lattice, the resulting rotational landscape bears 6-fold symmetry. The behavior described here is classical.

be delineated by Arrhenius behavior with 3-fold rotational barrier.

The reason why nuclear magnetic resonance is suitable for measuring the molecular rotation is that the energy imparted to the spin system would be subsequently transferred through the fluctuation[4] of local magnetic fields on the target nuclear spins and eventually to a thermal reservoir where the rotational degree of freedom accepts the energy. This process is termed spin-lattice relaxation, which is due to transverse components of the the fluctuating local fields. Namely, by inputting a perturbing energy and observing the relaxation behavior of the spin system, we are actually probing the rotation of the molecules that is thermally activated. In addition, depending on the size of a molecule and its rotational hindrance, the average rotational frequency of molecules ranges from 10^7 and 10^9 Hz, rendering NMR a natural measurement technique for probing rotation in a solid state since typical Larmor frequency of NMR is in the same range.

[4]The fluctuation is due to the randomness sourced from thermal reservoir.

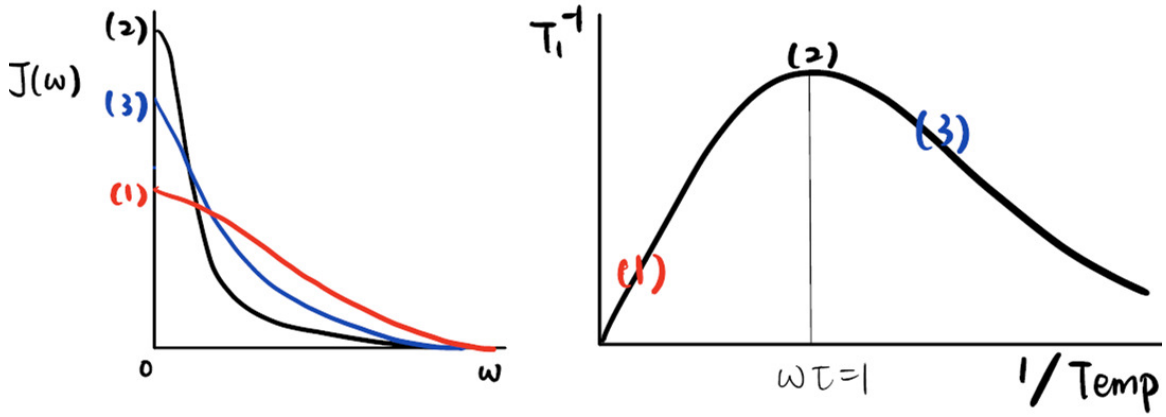

Figure 1.3: Left: spectral density as a function of angular frequency Right: spin-relaxation rate as a function of temperature. Since the number of molecules having rotational degree of freedom and participating in the relaxation process is fixed, the area underneath the curve of spectral density $J(\omega)$ as a function of carrier frequency ω is fixed. When the rotational frequency is equal to the Larmor frequency defined by the static magnetic field, the most efficient relaxation will result. By fitting the experimental spin-relaxation rate as a function of temperature to Kubo-Tomita relation, we can extract the activation energy and attempt-to-escape frequency of the rotation.

In a solid state sample, if there are molecules presenting fast rotation in an otherwise static matrix, spin-lattice relaxation would be controlled by the fast dynamic process. In addition, the energy barrier hindering rotations can be extracted from the temperature dependence of the spin lattice relaxation. The assumed thermally activated dynamic process can be delineated by Arrhenius behavior combined with the Kubo - Tomita equation

$$\frac{1}{\tau_c} = \frac{1}{\tau_0} exp(-\frac{E_a}{k_B T}), \tag{1.2}$$

$$\frac{1}{T_1} = C[\frac{\tau_c}{1+\omega_0^2\tau_c^2} + \frac{4\tau_c}{1+4\omega_0^2\tau_c^2}], \tag{1.3}$$

where $C = \frac{2}{3}\gamma^2 \boldsymbol{B}_{\boldsymbol{nuc}}^2$. $\boldsymbol{B}_{\boldsymbol{nuc}}$ is the local effective dipolar field. γ and ω_0 are the gyro-magnetic ratio and the angular Larmor frequency of the probed nuclei in an applied static magnetic field [24, 25]. A convenient way to fathom the Kubo - Tomita equation is illustrated in Fig. 1.3, which delineates that the most efficient spin-lattice relaxation occurs when $\omega\tau = 1$ is met. The behavior is a direct consequence of the fact that the number of rotating molecules accepting the relaxed energy is constant. The associated experimental details can be found in Appendix 4.2.2.1.

1.2 Introduction to Sr_2RuO_4 Project

In uncorrelated electronic system, electronic wave functions are extended in space and the system is in the quasi free electron regime due to strong overlap among wave functions. On the other hand, in a correlated electronic system, one has to consider Coulomb repulsions. Controlling the correlations from weak to strong limits results in profoundly different electronic properties, ranging from Fermi Liquid to Mott Insulator. Unconventional superconductivity is known to emerge in the presence of correlations. How that manifests in the special case of Sr_2RuO_4 motivates the exploration of this material by NMR methods.

1.2.1 Unconventional Superconductivity

Correlated behaviors have played essential roles in normal metallic state and superconducting state in many recently discovered and investigated superconductors. As a result, unconventional superconductivity has been a focal point in condensed matter physics. Emergent from the normal metallic state, superconductivity is associated with the pairing of states at the Fermi energy with time-reversed momenta. The spin state of the Coopers pair can be either singlet (total spin S = 0, anti-symmetric) or triplet (S = 1, symmetric), and due to the fact that electrons, being Fermions, have anti-commuting properties, the total wave function of Cooper pair must be anti-symmetric. In the case that spin-orbit coupling is not relevant, the total wave function of a Cooper pair can be expressed as

$$\psi_{total} = (\psi_{spin})(\psi_{orbital}). \tag{1.4}$$

With the aforementioned considerations, a singlet state, being anti-symmetric, is with symmetric orbital wave function such as s (angular momentum L = 0), d orbital wave function (L = 2), and so on, whereas triplet state being symmetric is accompanied by anti-symmetric orbital wave function such as p orbital wave function, f orbital wave function, and so forth. As described by Bardeen, Cooper, and Schrieffer (BCS), a conventional superconducting state with s-wave symmetry is typical where the pairing interaction is electron-phonon based. The order parameter is represented by a gap function $\Delta(\boldsymbol{k})$. For a s-wave superconductor, since the magnitude of the gap function is everywhere nonzero and the same sign, impurity scattering would not annihilate the gap function. On the other hand, for correlated system, on-site Coulomb repulsion prefers orbital wave function with larger probability amplitude away from origin to that at the origin so as to reduce the Coulumb repulsion energy. As such, higher orbital momentum is favored, corresponding to unconventional superconductivity $(p, d, f, ...)$, such as the high-T_c cuprate superconductors (d-wave).

Due to the symmetry of the orbital wave functions of $(p, d, f, ...)$, one characteristic of unconventional superconductivity is

$$\sum_{\boldsymbol{k}} \Delta(\boldsymbol{k}) = 0, \tag{1.5}$$

summing over the Fermi surface, which is accompanied by the fact that the coherence length equals to elastic scattering mean free path, namely elastic scattering rate equals to average energy gap.

1.2.2 Superconductivity in Sr_2RuO_4

Most superconductors discovered are spin singlet. Until now, spin triplet pairing is confirmed only in ^{3}He. As such, it is natural to be inquisitive about the possibility of electron spin triplet pairing, and what the defining disparities are between spin singlet and spin triplet. In addition, the possibility for entirely new superconducting state symmetries beyond s-wave was a natural outcome of the discovery of the high-T_c cuprates. In the case of cuprates, CuO_2 constitutes the 2-dimensional layer. In addition to cuprates, other transition metal oxides exhibiting the perovskite layered structure have been explored. However, Sr_2RuO_4 is not a high T_c superconductor, despite the closeness in structure with cuprate[5], as shown in Fig. 1.4. There are two main differences. Cuprates are characterized by a 3d filling close to $3d^9$ (odd number of electrons, $S = 1/2$[6]) whereas ruthenate has $4d^4$ (even number of electrons). Cuprates are Mott insulators, and become conductors only upon chemical doping. Sr_2RuO_4 is a good conductor without doping. In the 90's, the de Haas–van Alphen effect has been observed in Sr_2RuO_4, indicating its metallic normal state being a Fermi liquid. Together with other measurement results, a similarity to ^{3}He was recognized. Thus, an analogous triplet order parameter was also proposed. Measurements of the de Haas-van Alphen effect confirmed the strongly renormalized Fermi liquid properties of Sr_2RuO_4 previously inferred from thermodynamic measurements [26–30]. Among all correlated materials of interest, Sr_2RuO_4 is of particular importance because it is well considered to have chiral p wave order parameter, a topological superconducting state.

[5]For Sr_2RuO_4, T_c is lower than Fermi energy, whereas for high-T_c, T_c is higher than Fermi energy.

[6]on which quantum fluctuation is predicated

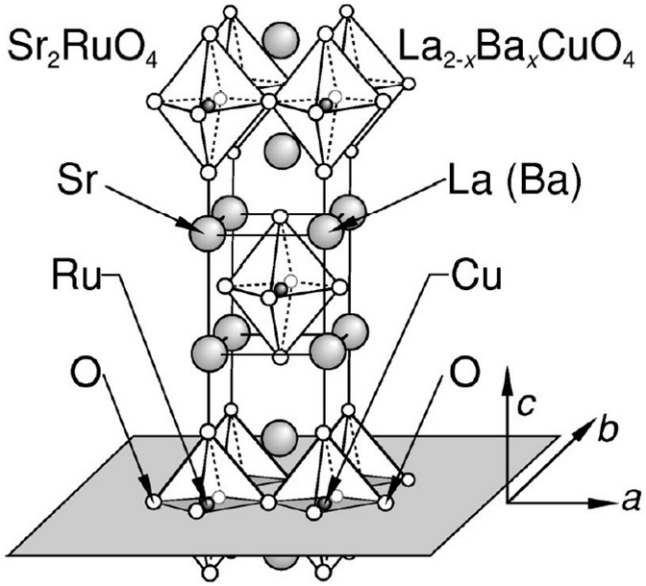

Figure 1.4: Sr_2RuO_4 has a quasi-two-dimensional perovskite structure the same as that of high temperature superconductor $La_{2-x}Ba_xCuO_4$ [2]. This commonality is one of the contributing factors for the nonfading interest in Sr_2RuO_4.

1.2.3 Objective of the Sr_2RuO_4 Research

The α, β, γ bands of Sr_2RuO_4 all cross the Fermi surface with evidence of strongly correlated characteristics associated with the partially filled Ru orbitals [29, 31]. With the observation of critical temperature equal to 1.5 K [32] and the indirect evidence for proximity to ferromagnetism, it was suggested that the pair wave function of the superconducting state likely to be a triplet [1]. Evidence aligned with this view included the inference, from NMR measurements, that there was no drop in electron spin susceptibility on cooling the system to T¡T_c. [5]. Together with experimental results indicating the presence of time-reversal-symmetry-breaking [33, 34], Sr_2RuO_4 is regarded as the the counterpart of a topologically nontrivial ^{3}He A phase [35] in the form of a charged superfluid, in the solid-state. Nevertheless, a consensus has not been completely reached since several measurements are not consistent with the proposed p-wave superconducting state [36–38]. For instance, the expected chiral edge current predicated on time reversal symmetry breaking has not been detected yet [39–41].

Symmetry considerations alone indicate that a chiral p-wave superconductor under uniaxial strain ϵ_{aa} (uniaxial strain along the a axis) is expected to have a split transition and a cusp, the behavior of T_c at $\epsilon_{aa} = 0$. Nonetheless, no such signs are found. Observed instead is an increase in critical temperature from 1.5 K to 3.5 K when ϵ_{aa} is tuned from zero to -0.5% [4], which is understood by considering a van Hove singularity associated with a peak of density of states at Fermi level [42]. The observation, including the uniaxial strain dependent critical temperature motivated a oxygen-17 NMR study, which indicated the peaking of density of states at the Fermi energy [43].

1.2.4 NMR on Sr_2RuO_4

Familiar to one's daily life,many of the properties of normal metals can be understood in the framework of the independent electron approximation and degenerate spin states, without the presence of Coulomb correlations [44]. After including strong correlations, exotic behaviors such as superconductivity are introduced, whose properties can be directly and indirectly accessed by NMR. For Sr_2RuO_4, we will primarily rely on NMR Knight shift to indirectly understand the order parameter of the superconducting state.

A direct probe to distinguish between singlet and triplet Cooper pairing for superconductivity is spin susceptibility. If a static magnetic field is applied to a material in the metallic state, the Zeeman shift of spin-up and -down states results in the polarization of the Fermi surface. The application of a magnetic field to a system of degenerate Fermions leaves the system polarized. On the other hand, there is no such response associated with the singlet superconductor. Thus, sufficiently high fields will destabilize the singlet superconductor in favor of the normal state. However, the susceptibility of the triplet superconductor can match the normal state, and is not destabilized by the applied field. NMR methods are sensitive to the spin polarization via the hyperfine interaction, and are therefore sensitive to the electronic polarization and can be utilized in distinguishing between pairing states.

Typically, the wave function of conduction electrons of p and d states have zero probability amplitude at the position of nuclei, so electron-nuclear spin interactions are dipolar and

therefore anisotropic. Another way in which conducting electrons convey with the nuclei is via the anisotropic dipolar interaction. The effective field resulting from the two interactions mentioned at the nucleus would determine the sign of hyperfine coupling constant and therefore dictates that of the Knight shift. In the case of Sr_2RuO_4, the dipolar interaction dominates the hyperfine coupling.

NMR Knight shift measures the frequency deviation from the Larmor frequency for the metallic and superconducting state. It has an orbital part $K_{orbital}$ and a spin part K_{spin}. K_{spin} is directly related to Fermi surface polarization and Pauli paramagnetic response of conducting electrons

$$\omega = \gamma B(1 + K_{orbital} + K_{spin}), \tag{1.6}$$

where ω is the resultant NMR peak position, γ is gyromagnetic ratio, B is the magnetic field experienced by the nuclei probed. Here K_{spin} is the integral proxy to investigate spin polarization as a function of temperature, and therefore to screen the type of Cooper paring, be it singlet or triplet. As shown in Fig. 1.5, the previous result pointed to triplet pairing [5]. In investigating uniaxial strain effects for the material, the expectation of chiral triplet p-wave order parameter was not found. In addition, in the absence of strain, our results conflicted with what is shown in Fig. 1.5.

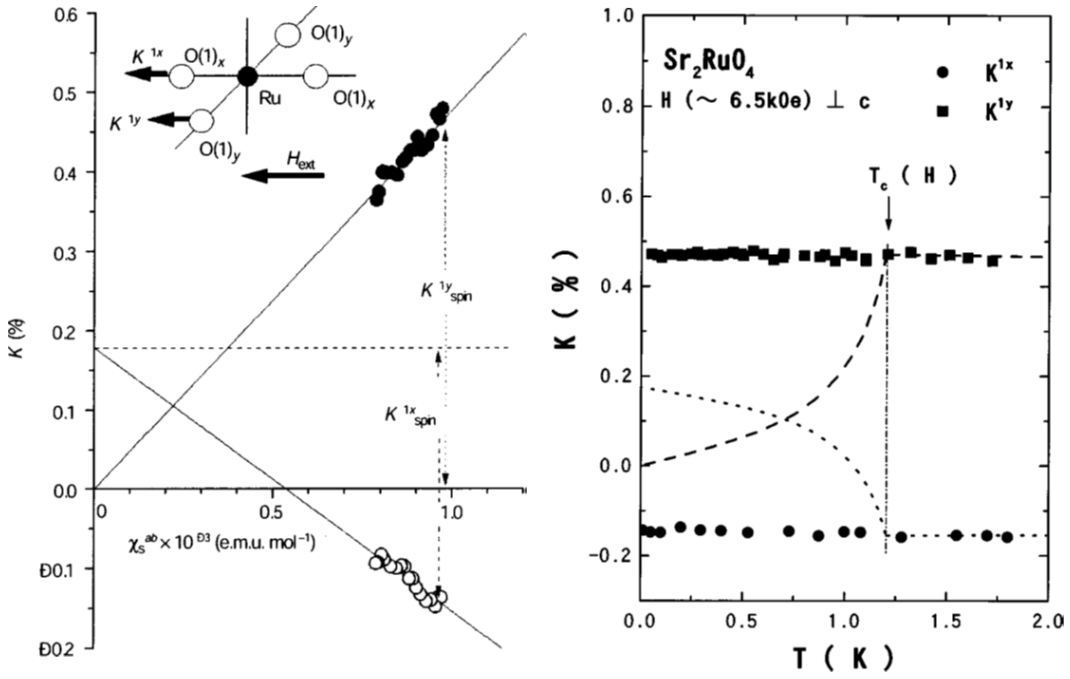

Figure 1.5: (Left) Total Knight shift as a function of DC spin susceptibility, which is proportional to temperature. It can be utilized to extrapolate the orbital part of Knight shift for the two oxygen sites. It also allows for evaluation of the hyperfine coupling constant. With static magnetic field applied in the ab plane, the spin part of Knight shift is not contingent on temperature, which points to triplet Cooper pairing. If the system is singlet d wave, the temperature dependence is calculated as shown as dashed lines in the right figure.

CHAPTER 2

NMR Fundamentals

Compared to techniques studying electronic properties on a macroscopic scale such as transport (eg: resistivity), optical (eg: photoemission), thermal (eg: specific heat), and magnetic measurements (eg: spin susceptibility), NMR is a probe that can be utilized to understand the local environment surrounding the nucleus. In addition, nuclear moments would not alter the electronic properties from which magnetic properties of the material are derived. As a result, it is non-invasive and can be used to distinguish effects on specific sites in the material.

2.1 Uncorrelated Spins in Static Magnetic Field

A nucleus is constituted by some number of protons and neutrons which are spin $\frac{1}{2}$ particles that amounts to different total magnetic spin $\boldsymbol{I}$

A nucleus has spin $\boldsymbol{I}$ that constitutes a magnetic moment $\boldsymbol{\mu}$ be related by gyromagnetic ratio γ_n

$$\boldsymbol{\mu_n} = \gamma_n \boldsymbol{I}. \tag{2.1}$$

With the application of a magnetic field, there exists an interaction between field and moment, which gives rise to the corresponding Zeeman Hamiltonian

$$H_z = -\boldsymbol{\mu_n} \cdot \boldsymbol{H_0}, \tag{2.2}$$

with its corresponding eigenvalues

$$E = -m\hbar\gamma_n \boldsymbol{H_0}, \tag{2.3}$$

where $m = -I, -(I-1), \ldots 0, \ldots, (I-1), I$, and there are 2I+1 levels equally spaced by $E = -\hbar\gamma_n \boldsymbol{H_0}$. This phenomenon is referred to as Zeeman splitting. Magnetic interactions allow for $\Delta m = \pm 1$ only, with the corresponding transition energy

$$\Delta E = -\hbar\omega_L, \tag{2.4}$$

where $\omega_L = \gamma_n \boldsymbol{H_0}$, coined as the Larmor angular frequency with which the independent nuclear spins presses around the applied magnetic field. ω_L is on the order of 10 MHz to several hundred MHz. And it is corresponding to a Zeeman temperature on the order of mK, which is smaller than room temperature (300 K) and Fermi Temperature (1000 K).

2.1.1 Rabi Oscillation

Consider a two-level system with two time independent eigenstates denoted in Dirac notation as $|0\rangle$, $|1\rangle$ and corresponding energies E_0 and E_1, which is thermally isolated. Any state on the Bloch sphere[1] can generally be represented by a superposition state of the system expressed as

$$|\psi(0)\rangle = A_0|0\rangle + A_1|1\rangle. \tag{2.5}$$

Following the application of the time evolution unitary operator U(t), its evolution of the superposition state can be expressed as

$$|\psi(t)\rangle = A_0|0\rangle + A_1 \exp\left(\frac{-i(E_0 - E_1)t}{\hbar}\right)|1\rangle. \tag{2.6}$$

Therefore, at a given time, the probability of finding the system in the initial state $|\psi(0)\rangle$ is $|\langle\psi(0)|\psi(t)\rangle|^2$. Now if we take $|\psi(0)\rangle = |1\rangle$ and turn on an oscillating transverse field with frequency $\omega_1 = \gamma_n H_1$ which engenders the time evolution, the probability of finding the vector state in $|1\rangle$ is

$$P(|1\rangle) = 1 - \left(\frac{\omega_1}{\Omega}\right)^2 \sin^2\left(\frac{\theta}{2}\right), \tag{2.7}$$

where $\theta = \Omega t$, $\Omega = \sqrt{(\omega - \omega_L)^2 + \omega_1^2}$, ω is transmit frequency, ω_L is the Larmor frequency. This equation captures the essence of Rabi oscillations. At resonance $\omega = \omega_L$, one gets the

[1] A geometrical representation that helps visualize any states of a two-level quantum system

optimal amplitude of Rabi oscillation corresponding to optimal signal amplitude; additionally, by applying $\theta = \pi$ pulse one can prepare $|1\rangle$ state from $|0\rangle$, whereas by applying $\theta = \frac{\pi}{2}$ pulse one can prepare a state in the plane perpendicular to the z axis such as $+\mathrm{x} = \frac{|0\rangle+|1\rangle}{\sqrt{2}}$ from $|0\rangle$, as shown in Fig. 2.1. In addition, the real and imaginary parts can be measured by quadrature detection described in Sec. 3.1.

2.1.2 Establishment of Thermal Equilibrium

If a system containing an ensemble of spins is in contact with a heat reservoir in thermal equilibrium, states with lower eigen-energies are preferentially occupied according to the Boltzmann distribution [45]

$$P(m) = \exp\left(-\frac{E_m}{k_B T}\right), \tag{2.8}$$

where $P(m)$ is the occupancy of each states. Due to the contact with the thermal reservoir, the population difference for each level amounts to a net nuclear polarization $\langle I \rangle$ and therefore a net magnetization of the spin system

$$M_z = N\gamma_n \langle I \rangle = N\gamma_n \frac{\sum_{-I}^{+I} \hbar m \exp\left(-\frac{E_m}{k_B T}\right)}{\sum_{-I}^{+I} \exp\left(-\frac{E_m}{k_B T}\right)} \sim \frac{N\gamma_n^2 \hbar^2 I(I+1)\boldsymbol{H_0}}{3k_B T} = \chi_n \boldsymbol{H_0}, \tag{2.9}$$

where N is the number of spins in the system, χ_n is nuclear magnetic susceptibility [46]. Due to the difference in mass between nuclei and electrons, the resultant difference in gyromagetic ratio and magnetic moment between the two species is large. Consequently, the nuclear magnetic susceptibility is 10^6 weaker than its electronic counterpart. Nevertheless, the nuclear magnetic response can still be probed spectroscopically with selective frequencies.

2.2 Relevant Interactions

Nuclear spins interact relatively weakly with their surroundings. Still, it suffices as a probe of condensed matter systems in the following ways. On one hand, interactions can serve as channels to probe the local surrounding environment of the selected nuclei, which are manifested in line splitting in the NMR spectrum. On the other hand, they are the channels

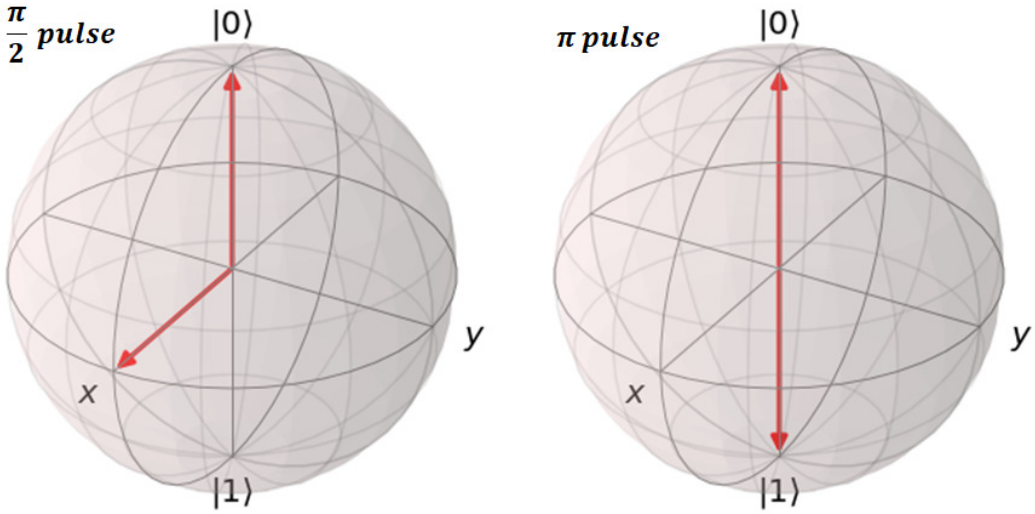

Figure 2.1: A large static field $\boldsymbol{H_0}$ applied along +z = $|0\rangle$ sets the initial condition of the spin ensemble, corresponding to thermal equilibrium. If a $\boldsymbol{H_1}(t)$ is along +y, a $\pi/2$ pulse will render the magnetization point along +x = $\frac{|0\rangle+|1\rangle}{\sqrt{2}}$, whereas a π pulse makes for the magnetization along -z= $|1\rangle$. A $\pi/2$ and a π pulse correspond to saturation recovery and inversion recovery techniques respectively to measure spin-lattice relaxation time. Left: the result of a $\pi/2$ pulse. Right: the result of a π pulse. After the preparation pulses, the polarization would recover to thermal equilibrium due to energy exchange with the thermal bath contacted with the quantum system. There could be different motional degrees of freedom in the bath that are responsible for accepting the released energy. In the case of the polar rotors presented in the thesis, the energy from the quantum system is accepted by rotational degree of freedom. It is the thermally random oscillating motion that oscillates the local magnetic field, which in turn induces the energy release. Software: QuTiP

through which energy is relaxed to the contacting thermal reservoir, with the associated spin relaxation times.

2.2.1 Dipolar Interaction

Dipolar interaction, typically on the order of kHz, involves two nuclear spins exerting a local field reciprocally, which is dependent on the magnitude of the vector separating the two spins that scales with r^{-3}, the angle between the vector and the static magnetic field (defined as the +z direction), and the magnetic moment of the respective spins which are directly proportional to their corresponding gyromagnetic ratio γ. In addition, since the angular frequency with which the spin experiencing the local field is rotated scales with γB_{loc} (think of the case where transverse oscillating field rotates the net magnetization with angular frequency γB_1), the resultant strength of the dipolar interaction depends on both γ's of the two participating spins. The general Hamiltonian of the dipole-dipole interaction can be expressed as[2]

$$H_{dd} = \frac{1}{2}\sum_{i=1}^{N}\sum_{j=1}^{N}[\frac{\boldsymbol{\mu_{ni}}\cdot\boldsymbol{\mu_{nj}}}{r_{ij}^3} - \frac{3(\boldsymbol{\mu_{ni}}\cdot\boldsymbol{r_{ij}})(\boldsymbol{\mu_{nj}}\cdot\boldsymbol{r_{ij}})}{r_{ij}^5}]. \tag{2.10}$$

The interaction among nuclear magnetic moments amounts to the homogeneous broadening of the associated resonant peaks in NMR spectrum, which is typically on the order of a few Gauss in a rigid crystal [47]. Actually it can lead to inhomogeneous broadening [48]. Finally, inter-nuclear coupling promotes a uniform spin temperature, meaning that the nuclear spins are in thermal equilibrium.

2.2.2 Hyperfine Interactions

2.2.2.1 On-Site Hyperfine Coupling

The interactions between nuclear spins and magnetic moment associated with electrons are known as hyperfine interactions as a group [45, 47]. The dipole-dipole interaction between

[2]Thermal energy could create fluctuation in the distance between two spins and/or in angle dependence embedded in the numerator.

a nuclear spin I and an electron spin S can be expressed as

$$H_{d_n d_e} = -\frac{\mu_0}{4\pi}\frac{\gamma_n\gamma_e\ \hbar^2}{r^3}[\boldsymbol{I}\cdot\boldsymbol{S} - \frac{3(\boldsymbol{I}\cdot\boldsymbol{r})(\boldsymbol{S}\cdot\boldsymbol{r})}{r^2}], \tag{2.11}$$

where γ_n and γ_e are the gyromagnetic ratios of the nuclei and electron. When r goes to zero, Eq.(2.11) diverges. Namely, electron probability ought to be zero at the nuclei for the equation to be valid. In this regard, p, d, f shells electrons are plausible, but not so for electrons in an s-state.

For s shell electrons, the associated interaction is coined contact interaction

$$H_c = \frac{\mu_0}{4\pi}\frac{8\pi}{3}\gamma_n\gamma_e\ \hbar^2[\boldsymbol{I}\cdot\boldsymbol{S}\ \delta(\boldsymbol{r})], \tag{2.12}$$

where for a nucleus at $r = 0$, r indicates the site of nuclei. In metals, the hyperfine interaction leads to the Knight shift K

$$K = \frac{\mu_0}{4\pi}\frac{8\pi}{3}\gamma_n\gamma_e\ \hbar^2\frac{\chi_{p_0}}{g\mu_B\hbar\gamma_n}, \tag{2.13}$$

where χ_{p_0} is the Pauli susceptibility

$$\chi_{p_0} = \frac{1}{2}(g\mu_B)^2\rho(E_F), \tag{2.14}$$

and $\rho(E_F)$ is the electron density of states at Fermi level. In addition, the value of K depends on nucleus. For instance, hydrogen has very small couplings. A heavy nucleus like an actinide could be much larger. Oxygen in SRO is of order 0.5% and less. The interaction corresponding to the magnetic field originated from electron orbital angular momentum can be expressed as

$$H_{orb} = -\frac{\mu_0}{4\pi}\gamma_n\gamma_e\ \hbar^2\ \frac{\boldsymbol{I}\cdot\boldsymbol{l}}{r^3}, \tag{2.15}$$

where $\boldsymbol{l}$ is associated the loop electron current induced by applied magnetic field. When an external magnetic field is applied, occupied and unoccupied orbitals can mix, forming a current loop orthogonal to the applied field, resulting in a local magnetic field at the nuclear site. Hence, it is of anisotropic nature. In addition, the effect is on the order of ppm, but can be much larger, particularly in transition metals where it commonly depends on the crystal field effects on the d orbitals. On the other hand, in the case that the time

fluctuation of hyperfine field is faster than the Larmor frequency, all the above electronic hyperfine interactions are essentially an effective time averaged magnetic field B_{eff} acting on the nuclear spin[3] [49]

$$H_{eff} = -\gamma_n \hbar \, \boldsymbol{I} \cdot \boldsymbol{B_{eff}}. \tag{2.16}$$

2.2.2.2 Transferred Hyperfine Coupling

In additional to the on-site hyperfine coupling, the nuclei in question are also influenced by electrons on its neighboring sites through the exchange interaction with intermediate itinerant electrons

$$H = -J \, \boldsymbol{S} \cdot \boldsymbol{s} \, \delta(r), \tag{2.17}$$

where J is the exchange coupling strength, S is the on-site nuclear spin, and s is itinerant electron spin. Therefore, the total hyperfine coupling that includes both contributions is denoted as

$$A(\boldsymbol{q}) = A_0 + \sum A_i e^{i\boldsymbol{q}\cdot\boldsymbol{r_i}}, \tag{2.18}$$

where A_0 represents total contribution of the on-site hyerfine coupling, and the second term delineates the $\boldsymbol{q}$ dependent transferred hyperfine coupling, with A_i decaying strongly with distance and it suffices to consider only the first-nearest-neighbor (NN).

The various local field contributions sum to influence the resulting spectrum; the perturbations are summarized qualitatively as follows. Zeeman splitting is the dominating factor in determining the resonance frequency. Hyperfine interaction shifts the resonant peak. Quadrupole and dipolar couplings further split or broaden the peaks. The NMR spectrum can be regarded as a map to understand the interactions felt by the target nucleus in its immediate adjacent local environment.

In the rotor project, the most relevant interaction is the inter-nuclear dipolar interaction that triggers spin-lattice interaction, whereas in the Sr_2RuO_4 work we are most interested in the hyperfine interactions and the associated Knight shift K. In addition, while the

[3]Note that there is also a diamagnetic part to the chemical shift which is also a contributor to B_{eff}.

interaction that is fluctuating along z axis would lead to spin-spin relaxation (dephasing), transverse fluctuations give rise to spin-lattice relaxation (energy exchanged with a thermal reservoir).

2.3 Spin-Lattice Relaxation

In a pulsed NMR measurement, a static magnetic field is applied in the +z direction, and a transverse RF $\pi/2$ pulse at the Larmor frequency is applied, rotating the net nuclear magnetization toward the -y direction, which is then followed by energy relaxation back to thermal equilibrium. While the excitation is triggered by a resonant RF pulse of the Larmor frequency homogeneously experienced by all spins, the relaxations are initiated by fluctuating local fields that contain transverse components, which varies for individual spins. One common source of fluctuating local fields is magnetic dipolar interaction with vibrational or rotational degree of freedom. The local fields are varying vectors arbitrary both in direction and amplitude, with randomness from thermal fluctuation of motions of nuclei participating in the dipolar interaction. If the thermally agitated motions (eg. vibration and rotation) of molecules amount to fluctuating local fields, the spins influenced by the fields would exchange energy with the thermal reservoir and re-establish the equilibrium. The time evolution of the z magnetization starting from the perturbed state back to the reference equilibrium state is coined spin-lattice relaxation, with the term lattice meaning equivalently to thermal reservoir.

2.3.1 Thermal Randomness

In most solids, only the vibrational phonon modes are relevant. The rotors system are special in that rotational degree of freedom are purposely built in. The above two degrees of freedom are the sources of thermal randomness that drive the corresponding fluctuating local fields. While vibration quite often takes on the frequency range between 10^{11} and 10^{13} Hz, rotation falls in the range from 10^7 to 10^9 Hz. As far as nuclear magnetic resonance is concerned,

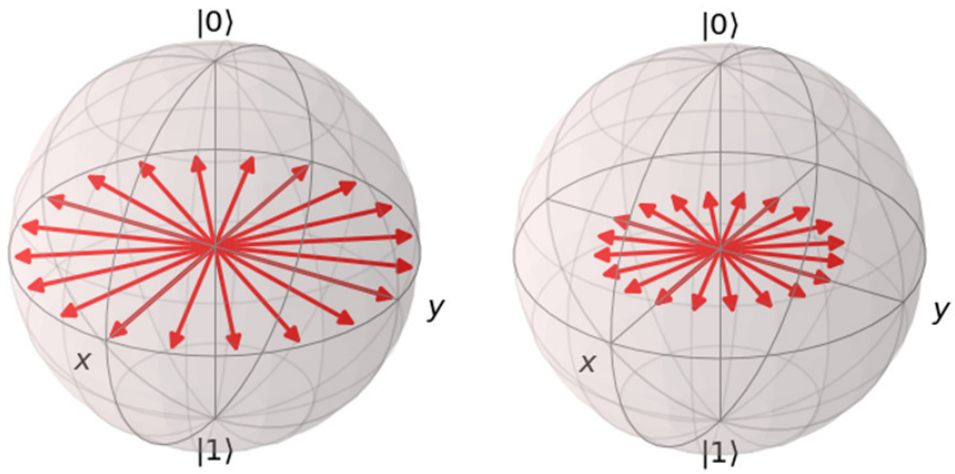

Figure 2.2: While a spin system is re-establishing thermal equilibrium, the total magnetization is rotating back to $|0\rangle$, during which process energy is exchanged with the environment, and the process is manifested as the dwindling in magnitude of the dephasing x-y components. Left: pure dephasing without energy loss. Right: pure dephasing coupled with energy loss. While dephasing can be refocused, energy loss to thermal bath is not reversible. Spin-lattice relaxation can also be regarded as an information-loss process. Software: QuTiP

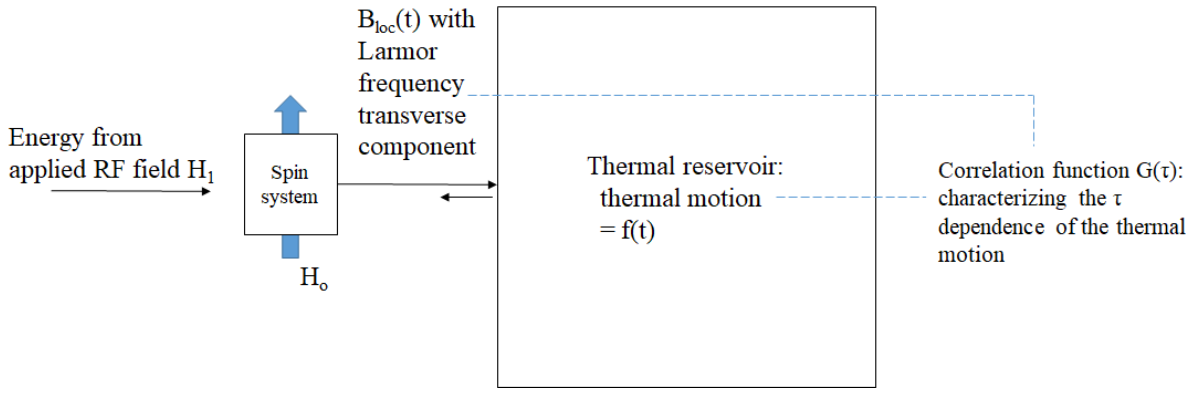

Figure 2.3: Zeeman interaction first lifts spin degeneracy, followed by a transverse field of Larmor frequency that creates population inversion making the quantum system to be in an excited state. Due to fluctuating transverse local field at Larmor frequency serving as the bridge to thermal reservoir, thermal equilibrium is re-established [7]. Note that if the local field is deviated from Larmar frequency, less efficient will be the energy release. Thermal reservoir, or equivalently the lattice, is a collective term that includes motional degrees of freedom such as translation, rotation, and vibration. Thermal equilibrium governs the detailed balance relationship $\Gamma_{1\uparrow}/\Gamma_{1\downarrow} = exp(-\hbar\omega_L/k_BT)$ and the net polarization can be approximated as $\tanh(\hbar\omega_L/2k_BT)$ [8].

the Larmor frequency overlaps with that of rotational degrees of freedom; as such, rotation is the dominant source of relaxation.

In condensed matter, since there are various sources of interaction that inform an energy barrier for reorientation, the resultant motion would take on a wiggling approach which is regarded as diffusional reorientation. A timescale associated with the activated behavior is the correlation time τ_c (second/rad), meaning the average time for all molecules to reorient by 1 radian. To initiate spin-lattice relaxation, the local fields must have transverse component with Larmor frequency. In order to quantify the amount of molecules of certain rotational frequency that in turn defines the frequency of their corresponding local fields, spectral density $J(w)$[4] enters the picture, which is directly linked to the frequency distribution of density of rotational degrees of freedom that receive relaxed energy. Consider two spins which assumed random[5] motion with respect to one another, an auto-correlation function decaying as

$$\exp(-\frac{t}{\tau_c}), \tag{2.19}$$

can be assumed to describe the extent of correlation with each other. The Fourier transform of the auto-correlation function is spectral density, which takes on the form[6] [7]

$$J(\omega) = G(0)\frac{2\tau_c}{1+\omega^2\tau_c^2}, \tag{2.20}$$

where τ_c is the correlation time, $G(0)$ is the correlation function at $t = 0$. An essential feature of $J(\omega)$ versus ω plot is that the area underneath the curve is contingent on strength of local fields $G(0) = \overline{|\langle f|H'|i\rangle|^2}$ and is irrespective of varying τ_c that could be diffusive. This feature leads to an integral characteristic of $J(\omega)$ versus τ_c, in which $J(\omega)$ has its maximum value when $\omega\tau_c = 1$. This behavior directly manifests in the spin-lattice relaxation rate. As

[4]A correlation function can be assumed to derive spectral density, for which the reader is invited to refer to Appendix 6.2. It serves as a measure how fast the local interaction changes its magnitude and direction till entropy dominates the story, predicated on the assumption that the time variation of motion is random.

[5]Compared to the randomness in the quantum world dictated by uncertainly principle, the randomness here is classical where in principle one is able to determine a associated probability.

[6]Put in another way, time dependent interaction energy between the two spins can be isomorphically[7] translated to frequency dependence of the interaction power, namely spectral density.

shown in Fig. 6.1, when $\omega\tau_c = 1$, the amount of molecules reorienting at Larmor frequency peaks, and as a result this is the condition where spin-lattice relaxation is most efficient.

2.3.2 Fermi's Golden Rule

In general, energy can be released to the lattice through spontaneous and simulated relaxation. At radio frequencies, spontaneous emission is insignificant in that its probability is proportional to $f^{\frac{1}{3}}$, and stimulated emission is predominant [46]. As such, the rate is contingent on the strength of the perturbing fields therefore the magnitude of matrix element between initial and final states. It is dependent on the density of final state (degree of freedom) at Larmor frequency. [8]. Fermi's Golden Rule delineates the energy transfer probability from initial state to final due to certain perturbing coupling, and can be expressed as

$$\Gamma_{i\to f} = \frac{2\pi}{\hbar}|\langle f|H^{'}|i\rangle|^2 g(\hbar\omega), \tag{2.21}$$

where $\Gamma_{i\to f}$ is the decay probability, $H^{'}$ is the fluctuating local field coupled to the xy plane[9]. $g(\hbar\omega)$ is the density of final state at certain frequency.

2.4 Spin-Spin Relaxation

Frequently referred to as transverse relaxation or transverse phase decoherence, spin-spin relaxation is associated with phase memory of the system being scattered when like spins have energy-preserving spin-flips with one another, typically due to dipolar interaction between nuclear spins.

There are two contributions to spin-spin relaxation, the secular part and the non-secular

[8] If there are multiple coupling mechanisms at play, the corresponding relaxation rates can be added directly. This is under the assumption that there is no correlation among the motional degrees of freedom; otherwise, often a stretched- or non-exponential relaxation results

[9] The interaction Hamiltonian must have time-varying off-diagonal elements. In general, a Hamiltonian containing no time dependent elements has time translation symmetry. And it means that the energy of the system is conserved.

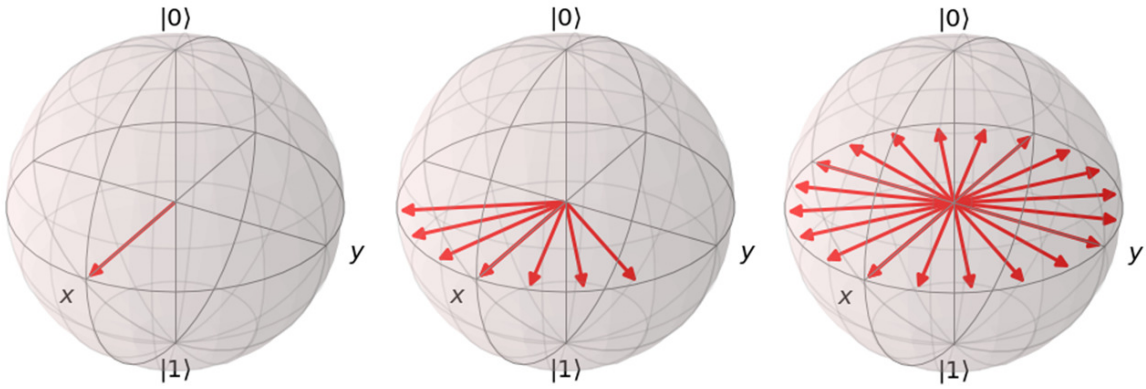

Figure 2.4: The pure dephasing process. It amounts to the envelope of free-induction decay. In addition, it is due to the longitudinal (along the quantization axis, z) fluctuation of local field. The pure dephasing process can be re-phased or re-focused by a spin-echo pulse sequence. Namely, no energy or information is lost to the thermal reservoir. Software: QuTiP

part.[10] The secular part derives from the fact the z components of fluctuating local fields would modulate the original static field $\boldsymbol{H_0}$. As a result, the nuclear spins are generally subjected to a distribution of effective static field, and there exhibit a distribution of precession frequencies. Hence, over time the spins would become out of phase to one another. The time scale of the secular part is often denoted as T_ϕ.

On the other hand, the non-secular part originates from the fact that while the transverse component of local fields at Larmor frequency couple to the x or y component of the spins and therefore reorient the net magnetization toward z direction, namely thermal equilibrium. In this case, not only the z magnetization is changed but also the transverse magnetization is altered. In essence, this is exactly spin-lattice relaxation [7].

Collectively, the overall contribution to spin-spin relaxation rate $\frac{1}{T_2}$ can be expresses as

$$\frac{1}{T_2} = \frac{1}{T_\phi} + \frac{1}{2T_1}, \tag{2.22}$$

[10]Due to mutual spin flip, no energy relaxation is associated with the secular part, whereas non-secular part do not have mutual spin flip there is corresponding to spin lattice relaxation and energy is released to thermal reservoir.

where the factor 2 comes from the two spatial degrees of freedom of xy plane. In comparing the two contributions, the secular pure dephasing part can be caused by fluctuation modes of broad bandwidth, the nonsecular spin-lattice relaxation part is subject to only fluctuating modes of very narrow bandwidth since it is a resonant phenomena. While the former is reversible, the latter is not. In the absence of inhomogeneous broadening[11], $1/T_2$ is proportional to linewidth. Based on the Redfield analysis [45], the secular linewidth is related to correlation time τ by

$$\frac{1}{T_\phi} = \gamma_n^2 H_z^2 \tau, \tag{2.23}$$

$$\tau = \tau_0 \exp(\frac{E}{k_B T}), \tag{2.24}$$

where τ_0 is attempt-to-escape correlation time and E is activation energy for random walk. We can see the lower the correlation time which leads to slower dephasing, the narrower the width. The phenomena is commonly referred to as motional narrowing. The relationship applies in the regime $\frac{1}{T_\phi} \leq \frac{1}{\tau}$, where an activated jump happens before a spin dephases by one radian. On the other hand, when $\frac{1}{T_\phi} \geq \frac{1}{\tau}$, the dephasing rate is faster than the activated perturbation. Hence the dephasing becomes independent of τ and therefore temperature independent. We can map the effects on linewidth of $1/T_\phi$ and $1/T_1$ into the same plot as shown in Fig. 2.5. The secular part of the transverse relaxation plays an integral role in the resultant NMR spectrum linewidth. Predicated on the spatial variation of local fields throughout the sample concerned, a spatial distribution in Larmor frequencies is expected. In this regard, in the limit of very slow molecular motion $T_\phi \leq \tau$, the local field experienced by an individual spin can be regarded as bearing nearly no time dependent variation. As a result, concerning all the spins, the spread in Larmor frequencies would be reflected as a relatively broad line in NMR spectrum. Conversely, in the limit of fairly fast molecular motion $T_\phi \gg \tau$, since an individual spin incessantly and expeditiously change from one position to another, the local field experienced by an individual spin would be informed as the time average of those at each position. As such, an average of Larmor frequencies results,

[11] Inhomogeneous broadening results from a spatial dependence of local fields in the material.

which would be manifested as a comparatively narrow line in NMR spectrum.

If we consider two same-spin-1/2 nuclei bearing random motion, the dipolar interaction between them can be expressed as Eq. 2.10, which can be further massaged by automorphically transforming to spherical coordinate and in the quantum language with a associated Hamiltonian as

$$H_{dd} = \frac{\hbar^2 \gamma_{n1} \gamma_{n2}}{r^3}(A + B + C + D + E + F), \tag{2.25}$$

where aside from angle dependence, the five terms have the following properties: $A \sim (I_{1z} I_{2z})$ corresponds to the diagonal terms without any spin flip, $B \sim (I_1^+ I_2^- + I_1^+ I_2^-)$ is off-diagonal that corresponds to mutual spin flip, off-diagonal C, D correspond to only single spin flip associated with energy transfer $\sim \omega$, off-diagonal E, F correspond to two spin flipping in the same fashion associated with energy transfer $\sim 2\omega$. As a result, C, D, E, F amount to the spin-lattice relaxation rate that can be expressed in the form of

$$\frac{1}{T_1} = \frac{3}{2}\gamma^4 \hbar^2 I(I+1)[J^{(1)}(\omega) + J^{(2)}(2\omega)], \tag{2.26}$$

where $J^{(1)}(\omega) = (1/6)J^{(0)}(\omega)$, $J^{(2)}(\omega) = (2/3)J^{(0)}(\omega)$, $J^{(0)}(\omega) = (8/5r^6)[\tau_c/(1+\omega^2\tau_c^2)]$, which correspond to one, two, and zero spin flips [45, 46]. The engendering of Eq. 2.26 is equivalent to the derivation originally by Bloembergen, Purcell, and Pound using time dependent perturbation [50], and so it is coined BPP relaxation, which will be utilized to understand our rotors that are polarized by spin-1/2 ^{19}F nucleus.

2.5 Pulse Sequences and Measurements

2.5.1 Free Induction Decay

By applying a $\pi/2$ pulse (on the order of a few μs), the spins ensemble is rotated to the xy plane and start to precess about the quantization axis (z) and dephase, which leads to free induction decay (FID). The dephasing is due to spin-spin relaxation and/or inhomogeneous environment. The associated time scale is T_2. The FID in the time domain can be Fourier transformed into the frequency space leading to our NMR spectrum.

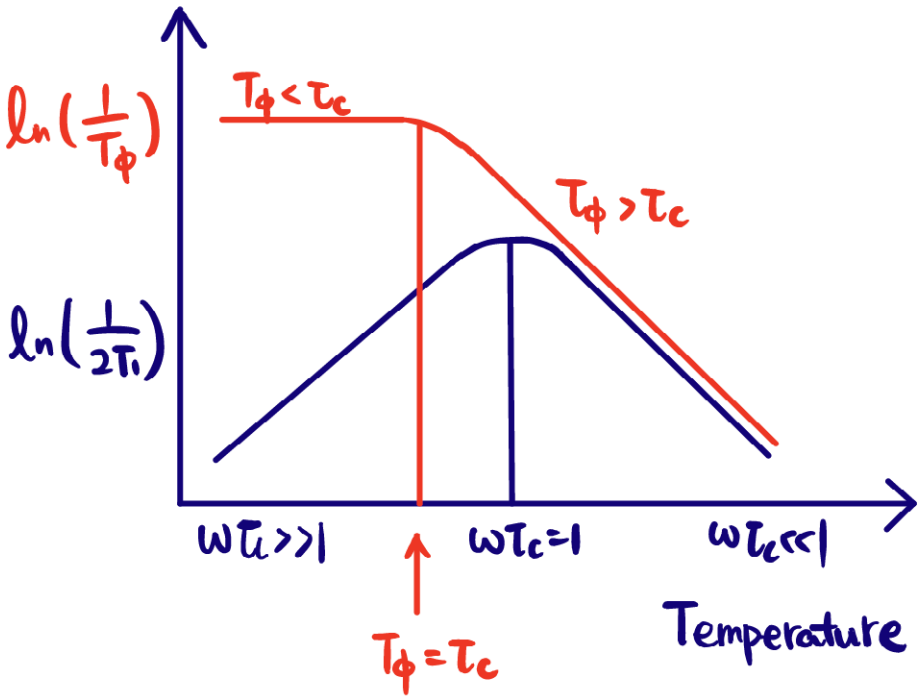

Figure 2.5: Schematics of temperature dependent linewidth, contributed by dephasing and T_1 processes. Red: the temperature dependence of T_ϕ is the reason for motional narrowing (increasing temperature) or linewidth broadening (decreasing temperature). At higher temperature where $T_\phi > \tau_c$, the longitudinal fluctuation is thermally-controlled because the underlying dynamic is faster than the dephasing. By pinpointing the crossover point, we are able to determine the correlation time of the system's major dynamic. Blue: the T_1 contribution. When the underlying dynamic frequency is equal to measurement frequency, the most efficient spin lattice relaxation results. Incidentally, the same spirit can also be found in the Debye model of relaxation, where a loss tangent peak occurs when $\omega\tau = 1$ is met. We will see in the rotor project that the above-mentioned are utilised together to understand the dynamics of the system, with the help from DFT calculation.

Practically, inhomogeneity in external magnetic field would contribute to dephasing too. Another practical point is that a pulse width is corresponding to a certain transmission bandwidth, indicating the range of frequencies that can be excited. The correspondence can be taken as $\Delta\omega = 0.5 \times (pulsewidth)^{-1}$. For instance, The effective bandwidth for a 3 μs $\pi/2$ pulse is around 165 kHz, which may not be sufficient to cover the spectrum in the case of extreme inhomogeneous broadening.

2.5.2 Spin Echo

The time scale T_2 varies considerably in solids. In the case of short T_2, artificial effect such as inhomogeneous magnetic field to be shorter than the recovery time of spectrometer after the pulse (often times the digitizer is the limiting factor), it becomes impossible to observe the expected FID when everything else is well prepared. One ingenious approach to overcome this issue is the spin echo proposed by Erwin Hahn in 1950. The pulse sequence is first applying a $\pi/2$ pulse, followed by the application of a π pulse after a waiting time τ that is shorter than T_2. The function of the π pulse is to rotate the spin ensemble by 180 degree. In effect, the π pulse refocuses the dephased spins, leading to a refocused signal after the π pulse by another time span τ.

In practice, the FID has larger signal than spin echo, but its signal would suffer from ringing down of different origins such as power amplifier and/or mechanical ringing of the tank circuit in the NMR probe. Although the spin echo has smaller signal, it an be applied in combination with phase cycling and circumvent artifacts [12]. However, the spin echo bandwidth is reduced relative to the FID measurement since you have a π pulse.

2.5.3 T_1 Measurement

One of the common approaches to obtain the spin relaxation time is saturation-recovery, where the nuclear spins are tipped by a $\pi/2$ pulse comb, consisting of a sequence of knock-

[12]Such as ringing down and other artifacts from the electronics right after the first pulse. In addition, you are able to clearly pinpoint where the signal is supposed to appear by designating the waiting time τ.

down-and-decoherence process, corresponding to a rotation angle of θ and a reduction factor $cos\theta$ for the z component for one cycle. Repeating the cycles renders z component close to zero. Subsequently, the comb is followed by an adjustable recovery time τ and signal acquiring pulse (either FID or spin echo mentioned in the preceding subsection). The acquired Fast-Fourier-Transform spectra of different τ would therefore amount to a saturation recovery curve, which will be simulated as a single exponential function of the for

$$M_z = M_0(1 - exp(-\frac{\tau}{T_1})), \tag{2.27}$$

assuming there is only one dominant spin-relaxation process. M_0 is the magnetization in the thermal equilibrium state corresponding to full recovery.

Another approach for T_1 measurement is inversion recovery where we replace the saturation pulse(s) with a inversion pulse. Namely, we rotate the spins by 180 degrees to the -z, and then allow for recovery toward thermal equilibrium, followed by an observation pulse sequence (FID/spin echo). An advantage of inversion-recovery is that it has a factor two greater magnetization recovery as compared to saturation -recovery, with the resultant improvement in signal-to-noise-ratio.

2.5.4 T_2 Measurement

Predicated on the discussion of spin echo, the refocused signal would appear τ after the second pulse. The time-dependent decay in the case of a motionally narrowed line is Lorentzian

$$I(2\tau) = I(0)exp(-\frac{2\tau}{T_2}), \tag{2.28}$$

which we can use to extract the T_2 value.

CHAPTER 3

Experiment Setup

3.1 NMR Elements

The hardware of NMR experiments is inclusive of the following major components: a magnet that ideally supplies a homogeneous static field, a probe that accommodates the tank circuit, which is used to transfer energy to target nuclei at Larmor frequency. The measurement electronics can be divided according to transmitter and receiver functions. The structure of the entire setup can be found in Fig. 3.1.

Magnet The superconducting magnet is ubiquitous to NMR experiments. It is made up of a superconducting coil with persistent current, providing a stable magnetic field. The coil remains in the superconducting state by situating in a liquid ^{4}He bath at $4K$. In our experiments, the superconducting magnet can cover the field range of $0 - 12$ Tesla.

Probe The NMR probe is essentially a holder accommodating related components such as transmission lines, loaded by tank circuit and antenna, thermometers and heaters related to temperature control. The tank circuit is the lumped element resonance circuit, which couples the RF field to the spin system (sample). In particular, the tank circuit is tuned to the Larmor frequency with adequate matching for energy transfer. The coil is placed with its axis (the direction of applied transverse oscillating $\boldsymbol{H_1}$) orthogonal to the static magnetic field $\boldsymbol{H_0}$. When a static magnetic field $\boldsymbol{H_0}$ is applied along the z axis and the alternating field $\boldsymbol{H_1}$ in the x-y plane, the coupling between the spin concerned $\boldsymbol{s} = \frac{\hbar}{2}\boldsymbol{\sigma} = \frac{\hbar}{2}(\sigma_x, \sigma_y, \sigma_z)$

and the magnetic fields can be expressed by the following operator

$$\hat{H} = \sigma_z H_0 + \sigma_x H_1 = \begin{pmatrix} H_0 & H_1 e^{-i\omega t} \\ H_1 e^{-i\omega t} & -H_0 \end{pmatrix}, \; H_0 >> H_1, \tag{3.1}$$

$$\sigma_x = \begin{pmatrix} 0 & 1 \\ 1 & 0 \end{pmatrix} \; \sigma_y = \begin{pmatrix} 0 & -i \\ i & 0 \end{pmatrix} \; \sigma_z = \begin{pmatrix} 1 & 0 \\ 0 & -1 \end{pmatrix}.$$

The off-diagonal terms would induce transitions between eigenstates[1].

Transmitter It is devised such that a proper pulse sequence can be sent to the tank circuit. To fulfill the purpose, a function generator outputs a continuous wave, which will be shaped to pulse sequence with designated time scales and duty cycle. The pulse output is amplified to high power levels (up to the order of 100 watts) for proper H_1 field strength. Ideally, the output power transmitted to the tank circuit is such that the condition Eq. 3.2 is met with $t_{\pi/2}$ is of order 1 us[2].

$$\gamma_n \boldsymbol{H_1} t_{\frac{\pi}{2}} = \frac{\pi}{2}, \tag{3.2}$$

where γ_n is the gyromagnetic ratio of the target nuclei, $\boldsymbol{H_1}$ is the transverse oscillating field delivered through the sample coil to prepare the sample in excited state.

Receiver The tank circuit coil serves to detect the precessing magnetization[3] via an inductive coupling. This is transmitted to the receiver electronics via the transmission line and low-noise pre-amplifier.In particular, to hinder larger reflected power from getting to spectrometer and possibly cause any potential damage, there is a double diode in parallel with the low noise pre-amplifier. The double diode is shorted to ground, and only allows high voltage pulse to pass. As a result, instead of proceeding to receiver, the high power pulse will be reflected back from the double diode, along $\lambda/4$ coaxial cable again and eventually be in phase with the pulse being delivered to the sample.

[1] predicated on time-dependent perturbation theory

[2] The tipping process is part of Rabi oscillation as described in Eq. 2.7.

[3] small RF field signal on the order of μV radiated from the sample

Entering the receiver, the signal is mixed down in quadrature prior to digitization. If a single free induction decay signal with Larmor frequency $A\ cos(\omega_L t)$ is mixed with a receiver mixing frequency $B\ cos(\omega_{rm} t)$, the output of the mixer will be

$$(A\ cos(\omega_L t))\ (B\ cos(\omega_{rr} t)) = \frac{1}{2}\ AB\ [\ cos(\omega_L + \omega_{rr})t + cos(\omega_L - \omega_{rr})t\ ], \tag{3.3}$$

where A is associated with a decay function, and B is constant. The resultant high frequency part will be filtered out by a subsequent low pass filter. The remaining low frequency part (surrounding zero frequency) bears the spectrum ranging on the order of kHz dictated by the strength of interaction between the target nuclei and its immediate surrounding. Our sampling rate t_{dwell}^{-1} is on the order of 2 MHz.

In order to distinguish between positive and negative frequencies, the norm is to implement quadrature detection. Quadrature detection utilizes two mixers, with local oscillator (reference) inputs set to have relative 90 degree phase shift. After separately passing through a low-pass filter, the two signal outputs serve as x and y components respectively. As an example, Eq. 3.3 represents the x whereas Eq. 3.4 represents the y

$$(A\ cos(\omega_L t))\ (B\ sin(\omega_{rr} t)) = \frac{1}{2}\ AB\ [\ sin(\omega_L + \omega_{rr})t - sin(\omega_L - \omega_{rr})t\ ]. \tag{3.4}$$

The x and y serve as the real and imaginary parts in the time domain after digitization[4]. The hardware configuration of the quadrature detection is shown in Fig. 3.1.

3.2 Measurement Protocol

The power and signal flow of the measurement is illustrated in Fig. 3.1. On the transmission side, a function synthesizer outputs continuous wave (CW) form of interest frequency, which will then be sent to spectrometer. In the transmitter side of the spectrometer, the CW is re-shaped to a designated pulse sequence, which is designed using a software script and then sent to the spectrometer by the computer through TTL box which fires high/low dc voltage

[4]Predicated on the x and y components, one can justify the existence of the peaks that are of the same amplitude and shape and symmetric to ω_{rr}, without being an artifact.

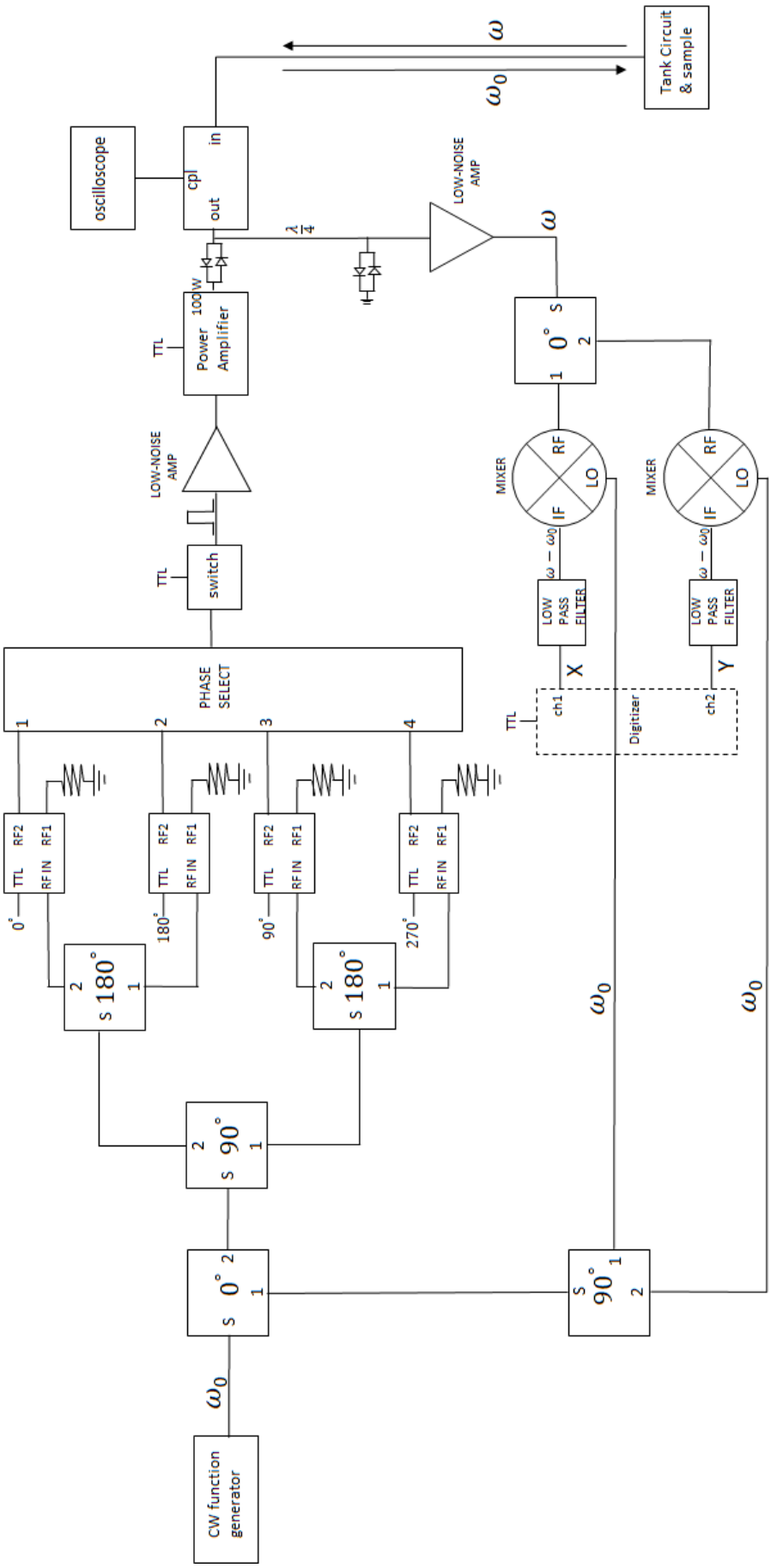

Figure 3.1: Schematic block diagram of routine NMR setup.

as triggers. The pulse sequence is then tuned to target power by using power amplifier and attenuators[5]. The purpose of the first double diode is to ensure unidirectional pathway of the transmission, blocking low amplitude reflections. Afterward, the directional coupler strips off 1% of the reflected power from the tank circuit for detection and circuit analysis purposes by the oscilloscope. By looking at the reflected power, one is able to gauge the situation of power absorption, quality factor of the resonant tank circuit (by looking at the number of oscillation at the decaying tail), and possible arching inside the measurement probe (observe whether there is real-time sparkling features). The tank circuit is a LC circuit resonator with tuning and matching elements. Our configuration is a tuning capacitor in series with sample coil and a parallel match inductance. Tuning is to move the resonance to the right frequency, while matching is to optimize the resonance. Notice that since the impedance of the tank circuit is contingent on temperature, one needs to take the temperature dependence into account before cooling down to low temperature.

On the receiver side, a quarter wavelength ($\lambda/4$) component is installed according to the transmit frequency, such that the portion of transmitted wave going through and being reflected by a second double diode would be in phase with the portion that goes directly to the sample. The second double diode is in parallel with the pre-amplifier to let all high power wave go through, without entering the pre-amplifier route which would damage the subsequent spectrometer.[6] Low noise pre-amplifer is in place since the signal coming out of the sample is relatively weak. Normally there are attenuators upstream the pre-amplifier due to the fact that the receiver side of spectrometer has a upper limit of power intake. After getting back to the spectrometer, the sample signal is split into two, which are respectively mixed with receiver reference CW waves that are 90 degree phase shifted. Ultimately, the two portions serve as the real part and imaginary part of the signal in time space, for the purpose of consistency check.

[5]Typical input power on the order of 20 - 100 W

[6]In addition, since this second double diode is shorted to ground, the high voltage wave reflected from the ground and reached back at the beginning of the quarter-wave-cable has been a phase difference of $e^{i2\pi}$, π due to reflection and another π due to going through quarter-wave-cable for two times, and therefore it is in constructive interference with the input power to the sample.

3.3 Tuning Scheme

A tank circuit is constituted by impedance elements including inductance and capacitance to form a resonant load that is 50 ohm matched to the carrier frequency. Contingent on the needs of experiments, one can adopt either a bottom-tuning or a top-tuning scenario. In the case of bottom-tuning, the tuning capacitance and matching inductance are in the vicinity of sample coil. An advantage of bottom-tuning is that it would keep the loss in the tank circuit to a minimum. Typically, the quality factor, and resulting signal/noise ratio, are greater for bottom-tuned circuits. Consequently, it is the ideal option when one needs to tackle the challenge of small signals due to low gyromagnetic ratio, low concentration of nuclei probed, or low static magnetic field. On the other hand, in top-tuning configurations, the tuning capacitance and matching inductance are situated out of the cryostat, which provides more tunability during the experiment, but it also necessitates a long co-axial cable that serves as part of the tank circuit amounting to additional resistive loss. In addition, one might be at risk of having destructive interference between the forward and reflected wave, or being misled by the resonant mode of in the added co-axial cable. Note that the phase shift of the reflected wave along the transmission line $= 2 \times 2\pi \times L/\lambda$. Destructive interference occurs when the top tuning cable length is odd multiples of $\lambda/4$. The schematics of bottom tuning and top tuning is illustrated in Fig. 3.2.

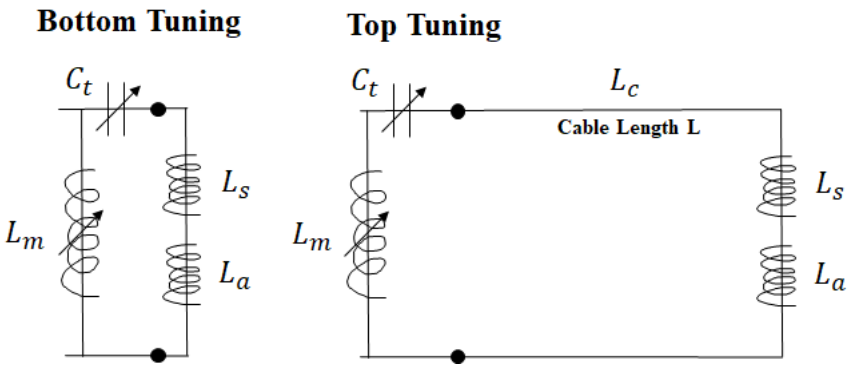

Figure 3.2: The schematics of bottom tuning versus top tuning setups. C_t is tuning capacitance, L_m is matching inductance, L_s is sample coil inductance, and L_a is the adjusting coil for better matching condition. For bottom-tuning, $\omega(L_s + L_a) = 50\Omega$, $L_m = (L_s + L_a)/\sqrt{Q}$, $Q = \sqrt{(L_s + L_a)/C_t}$; for top-tuning, the additional coaxial cable is part of your tank circuit, so the longer the cable the more energy loss one would encounter. $Q = \sqrt{(L_s + L_a)/C_t}/RL$, where R is the resistance per unit cable length. In addition, predicated on the carrier frequency, if $\lambda/2 >> L$, one could circumvent the risk of destructive interference or being misled by cable resonant mode. For sample coil, $Q_s = \omega_0\tau$, where $\tau = L_s/R_s \sim n^2/n$, and n is number of turns.

CHAPTER 4

Crystalline Polarized Rotors

4.1 Introduction

Crystalline arrays of molecular rotors present unique opportunities to explore emergent phenomena [14]. As an example, it is expected that 1D, 2D and 3D arrays of molecular rotors bearing interacting electric dipoles will spontaneously order, where the broken symmetry depends on the relation between the rotational axis orientation and the underlying lattice symmetry [51], in a manner analogous to that displayed by the arrays of macroscopic compasses depicted in Fig. 4.1 [6, 52]. For instance, 1D-dipole chains have a preferred ferroelectric alignment along the direction of the translation axis. Whereas, dipole orientation confined to a plane orthogonal to the translation axis leads to antiferroelectric ordering. Since the latter case constitutes a broken continuous symmetry, it is associated with a Goldstone mode: any orientation in the transverse plane is equally favorable. Similarly, the ground states of the ideal 2D and 3D arrays in Fig. 1 can adopt spontaneous ferroelectric or antiferroelectric order, and with one or more orientations that preserve the symmetry and energy of the assembly, enabling a range of applications associated with low energy long-wavelength excitations [53–55], or associated with the coupling to external fields [13, 56, 57], including electro-optic properties analogous to those of liquid crystals.

Classical order as depicted in Fig. 4.1 is generally expected when the thermal energy RT scale is of order the strength of the nearest-neighbor dipole-dipole interaction strength, E_{dd}. However, a state with considerable glassiness will result unless $E_{dd} \gtrsim E_a$, with E_a the variation in rotational potential associated with a dipole-lattice interaction and qualitatively illustrated in Fig. 4.2a. From these three factors, the experimental challenge is the design of

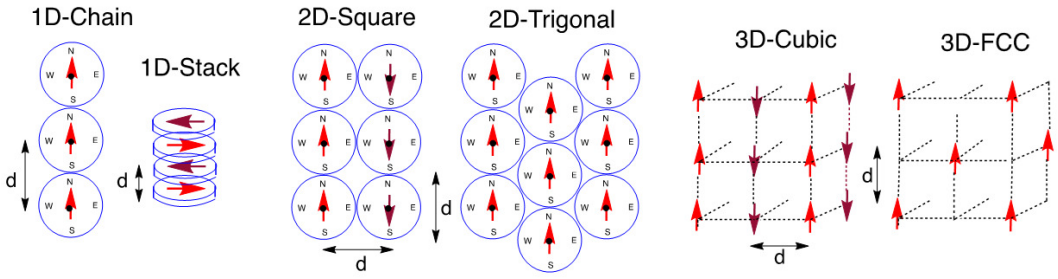

Figure 4.1: Broken symmetry states of classical rotary dipoles on lattices of different dimensionalities and symmetries, which can serve as the guidance that informs the expectation of possible emerging long-range order.

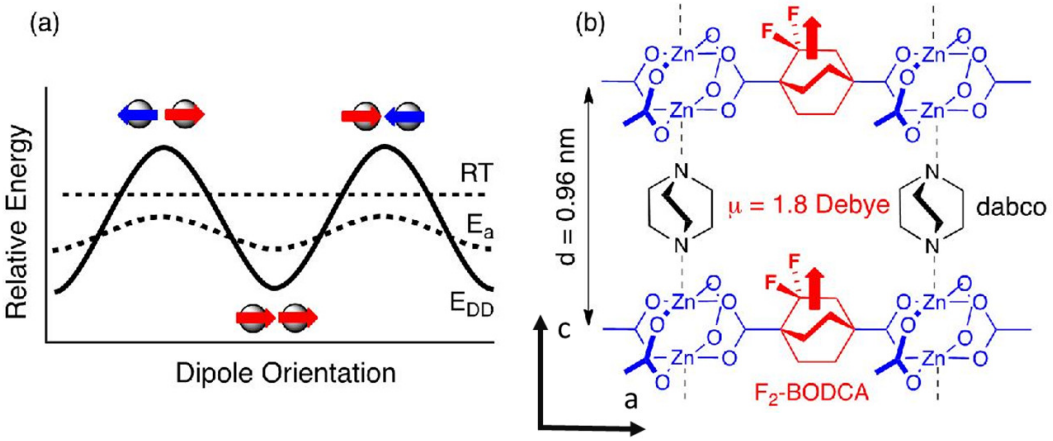

Figure 4.2: **a** Ideal conditions required for spontaneous dipolar order and correlated dipolar rotation, which are represented by two dipoles in a chain. **b** Line structure of the metal organic framework MOF $Zn_2(F_2\text{-BODCA})_2(\text{dabco-}H_{12})$ with polar 2,2-difloro-bicyclo-[2.2.2]octane-1,4-dicarboxylate rotators.

crystals with relatively low rotational barriers, which practically means that E_a is comparable to or ideally somewhat less than RT, with T corresponding to ambient temperature. If one specifically considers an ordering temperature of order 298 K or greater, one would need $E_a \lesssim 0.592$ kcal/mol, which implies rotational barriers on the same order of magnitude as the energy difference of a soft vibrational mode (*e.g.*, 207 cm^{-1} in this example). Fortunately, the solution to this challenge has been addressed systematically by us [17, 23, 58] and others [59–65], and a promising solution was recently found by taking advantage of metal organic frameworks (MOF) using a high symmetry bicyclo[2.2.2]octane rotator ($Zn_2(F_2$-$BODCA)_2$(dabco-H_{12})) [66], which was shown to have a barrier of only 0.2 kcal/mol (70 cm^{-1}). For this work, we selected the polar paddle wheel MOF $Zn_2(F_2$-$BODCA)_2$(dabco-H_{12}), consisting of layers of 2,2-difluoro-bicyclo[2.2.2.]octane-1,4-dicarboxylate (F_2-BODCA) rotators coordinated to dimeric zink(II) nodes with orthogonal 1,4-diazabicyclo[2.2.2.]octane (dabco) pillars that separate the layers. As described below, low-frequency dielectric and NMR spectroscopy measurements confirmed that the corresponding electric dipoles interact with the underlying lattice and with each other. At high temperature, the polar rotators are thermally disordered, and the dielectric response is Curie-Weiss-like, albeit with deviations close to T_c. A peak in the real part of the dielectric constant ϵ', observed at $T \simeq$100 K, is interpreted as evidence for a phase transition to an antiferroelectric state. The Curie-Weiss behavior is expected provided that the rotational potential is too large. This relationship is supported by Density Functional Theory calculations, which also provided the input for model Monte Carlo simulations performed on a square 2D rotary lattice.

4.2 Experimental

4.2.1 Dielectric Measurement

The dielectric measurements were carried out on a powder sample using a 3-terminal capacitance setup configured for audio frequencies at 300 Hz, 1 kHz, and 10 kHz, for temperatures covering the range T =20-270 K. Capacitance C and loss tangent $\tan\delta$ vs. temperature

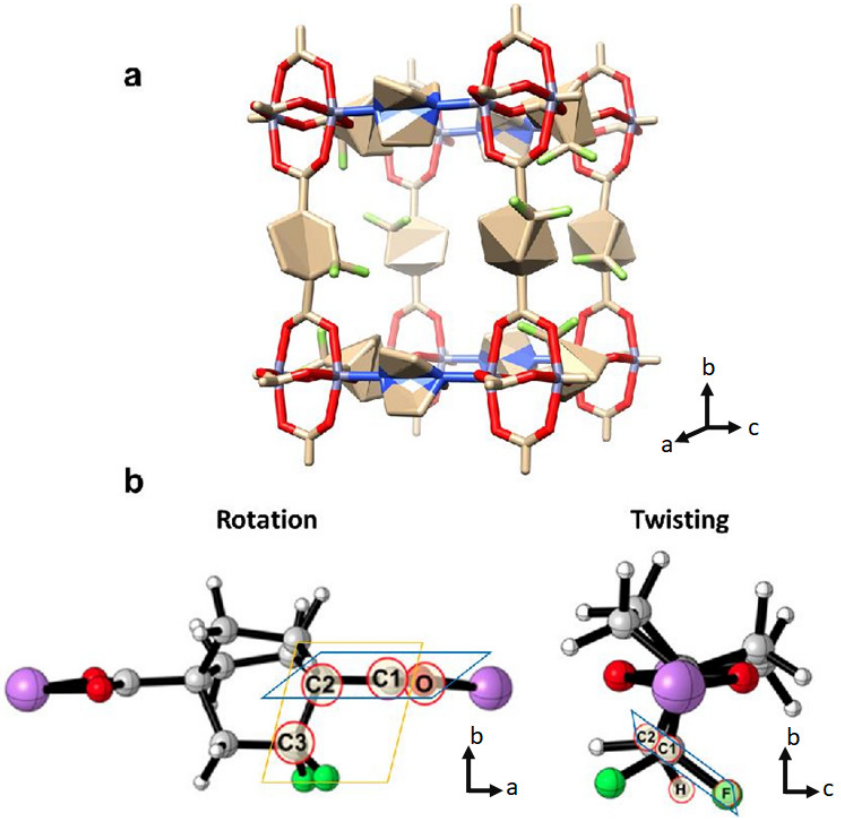

Figure 4.3: **a** Structure solution for the single crystal diffraction data of (F_2BODCA)-MOF at T=100 K, with a view near to the c-axis showing the positional and rotational disorder of the F_2BODCA rotors. **b** The M06-2X/6311+G(d,p) optimized structure of (F_2BODCA)-MOF. The rotation angle is between O-C1-C2 plane and C1-C2-C3 plane, whereas the twisting angle is between F-C1-C2 plane and C1-C2-H plane, respectively. The carboxylate groups (O-C-O) are coplanar and aligned along either the ac or bc crystal plane. [Figure courtesy of Ieva Liepuoniute]

are shown in Fig. 4.4, measured on a powder sample. The capacitance exhibits a cusp at $T \simeq 100$ K, with a weak decrease on further lowering temperature. This is followed by a sharp decrease below $35 - 45$K. A frequency-dependence is associated with the sharp decrease (and which is notably absent at higher temperatures). There is an accompanying loss peak in $\tan\delta$, which is also strongly frequency-dependent. Thus, the anomaly at T =100 K is interpreted as evidence for a phase transition, whereas the falloff in capacitance at lower temperatures is interpreted as a dynamical crossover.

Our goal is to extract some quantitative information from the dielectric response of the powder, which can then inform as to the rotator dynamics. From the crystal structure and ligand constraints, an anisotropic response is expected. With that caveat, we assume random grain orientation, and consider the angular average. Since the loss is relatively small at higher temperature ($T > 100$K), we take the capacitance as related to the plate geometry according to the elementary formula

$$C_p = \frac{K_p \epsilon_0 A}{d}, \tag{4.1}$$

where ϵ_0 is the permittivity of vacuum, K_p is the effective dielectric response of the powder, and A, d are area cross-section and distance between the plates, respectively. The packing density of the grains is less than 100%; our estimate, based on geometry and mass considerations is $\sim 65 - 70\%$. To account for the incomplete volume fraction α, we apply Böttcher's formula [67]

$$\frac{K_p - 1}{3K_p} = \frac{\alpha(K_s - 1)}{K_s + 2K_p}, \tag{4.2}$$

where K_s is the response for the sample. In isolating the response associated with the dipolar rotator degrees of freedom (χ_r) from what is expected to be a temperature- and frequency-independent background (χ_b), we rewrite the total as the sum of two distinct contributions, $K_s = 1 + \chi_r + \chi_b$. The rotator response χ_r is considered to follow a Curie-Weiss form at high temperature,

$$\chi_r = \frac{np^2}{2k_B\epsilon_0(T + \Theta)}, \tag{4.3}$$

with n the number of rotator per unit volume in the crystalline structure, Θ the Curie temperature, k_B Boltzmann constant, ϵ_0 vacuum permittivity, and p is the effective electric

dipole moment of the rotator. The factor 2 in the denominator is a geometric factor associated with the single-axis rotation. Following the subtraction of an inferred background, $\chi_r = K_s - (1 + \chi_b)$, with $(1 + \chi_b) \simeq 4.4$, $1/\chi_r$ *vs.* T is shown in the inset of Fig. 4.4a. Taking the high-temperature portion to be linear and using $\alpha = 0.7$, p=2.2 Debye is obtained. There is an approximate agreement with the calculated result, 1.8 Debye, previously obtained from the AM1 method using Spartan software [16], and is close to that derived from hybrid functional M06-2X/6-311+G(d,p) quantum mechanical method using Gaussian [68]. The characteristic temperature, as shown in the inset of Fig. 4.4a, is $\Theta = +150$ K.

As a means for parameterizing the frequency-dependent dielectric drop, Debye-like relaxation is assumed. Therefore, the real part K' and loss $tan\delta$ are expressed as

$$K' = 1 + \chi_b + \frac{\chi_r(0)}{1 + (\omega\tau)^2}, \tag{4.4}$$

$$tan\delta = \frac{\chi_r(0)\omega\tau}{[1 + \chi_b + \chi_r(0)] + (1 + \chi_b)(\omega\tau)^2}, \tag{4.5}$$

where χ_b is the background susceptibility, and $1 + \chi_b \simeq 4.4$ and $\chi_r(0)$=1.6 correspond to the real-part high and low frequency extrapolations, respectively, and ω is the angular frequency of the applied electric field. We find that the characteristic relaxation time τ follows a simple thermally activated behavior as:

$$\tau = \tau_0 \exp(\frac{\Delta}{k_B T}), \tag{4.6}$$

where Δ is an activation barrier for rotation. Loss peaks are determined by the condition $\omega\tau = 1$; where this condition is met is depicted in Fig. 4.9, with measurement frequency serving as an implicit parameter. The three lines are the expected variation for an activated relaxation process; the bold (green) line corresponds to $\tau_0 = 3.4 \times 10^{-10} s$, Δ=1.2 kcal/mol. As described below, complementary experimental information on rotator dynamics from ^{19}F NMR are consistent with a common relaxation process.

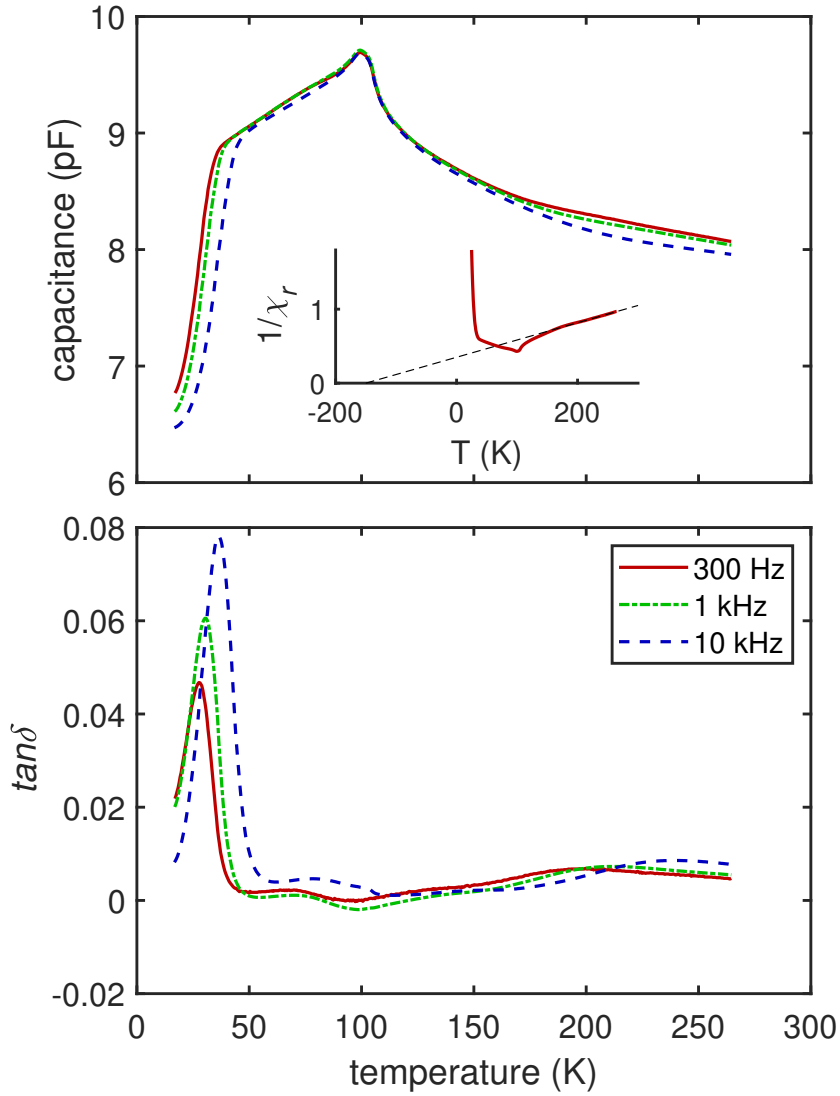

Figure 4.4: (a) Capacitance vs. temperature T, at reference frequencies f=300 Hz, 1 kHz, 10 kHz. *Inset:* Curie-Weiss analysis is consistent with overall antiferroelectric coupling, with an inferred background $1 + \chi_b \simeq 4.4$, Θ= +150 K (b) $tan\delta$ vs. T, measured at the same frequencies as the capacitance measurement. The most prominent feature is a substantial loss peak, which, for each frequency measured, is observed to occur at the crossover temperature in the real capacitance. The behavior is indicative of a dynamical freeze-out, which is understood in the framework of Debye-like relaxation.

4.2.1.1 Consideration of the Dynamic

To understand the frequency dependent feature surrounding 30 K - 50 K, Debye relaxation is assumed [69–71]. The extracted activated gap aligns reasonably well with the the results from DFT calculation, NMR spin relaxation time, and NMR linewidth, informing a self-consistent explanation that indicates the underlying dynamic to be a combination of twisting and rotation simultaneously. The results of loss tangents utilizing the simple Debye model are shown in Fig. 4.5, capturing the essence of the behavior observed experimentally.

To delve deeper into the understanding of the dynamics, a distribution in the activation energy is considered aiming to account for the observed difference in loss peak height at different measurement frequencies. Here we assume a normal distribution in activation energy, with the mean $\overline{E_a} = 600$ K taken from the correlation time indicated by Debye analysis and DFT calculation; standard deviations ranging up to $\sigma = 120$ K were attempted. An example of the effect of this additional distribution in activated gap is shown in Fig. 4.6. In addition, as shown in Fig. 4.8, we observe how the FWHM of the loss peak evolves as a function of the standard deviation of the distribution in activated gap.

In summary, the Debye analysis together with the results from DFT calculation and NMR measurements form a self-consistent description indicating the dynamic being a combination of twisting and rotation. Furthermore, the incorporation of a distribution in activated gap can account for up to 22 % difference in loss peak height whereas the FWHM of the loss peaks are close to those observed experimentally.

4.2.2 NMR Measurement

The temperature dependence over the range $T = 35 - 120K$ of the ^{19}F spectral Full Width at Half Maximum (FWHM), ($^{19}\delta\nu$) in Fig. 4.10 reveals that the broadening occurs in two steps upon cooling. The measurements were carried out at a field strength of $B_0 = 2.72$ T and carrier frequency 109.83 MHz. At temperatures $T \gtrsim 105$ K, the observed FWHM is ~ 13 kHz. As the temperature is reduced below 105 K, the FWHM is observed to increase before

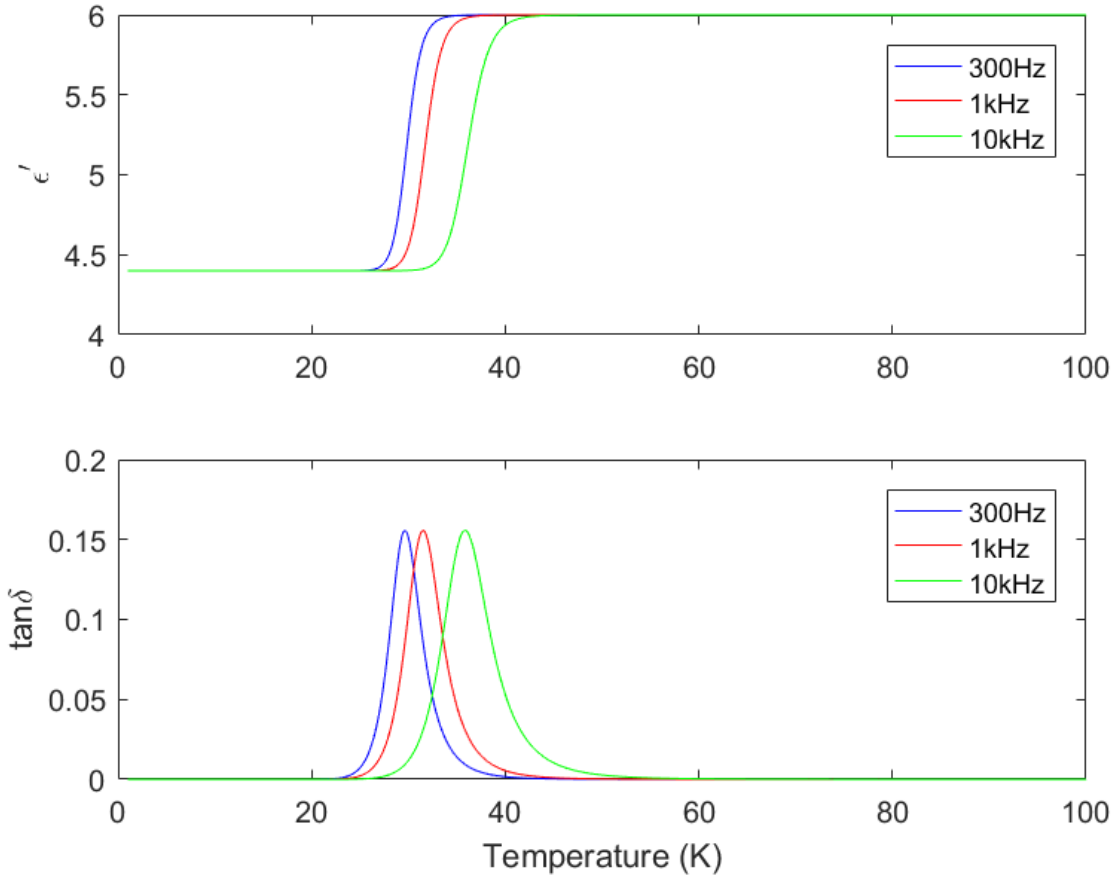

Figure 4.5: Upper: simulated real part of dielectric constant based on Debye relaxation. The absolute value of real dielectric constant is input from the experimental data, corrected by taking into account the empty space in the materials. Lower: simulated loss tangent based on Debye relaxation

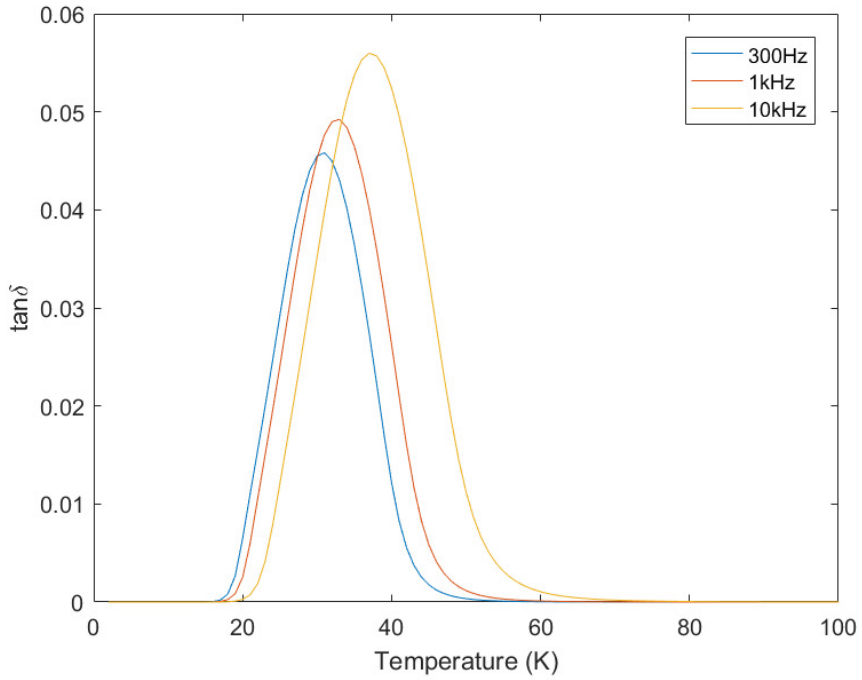

Figure 4.6: Simulated tanδ as a function of temperature. Attempts are made to account for the observed difference in tanδ peak height (Fig. 4.4) by including an additional distribution of activation energy of dynamics. This example figure demonstrates the modified Debye-relaxation resulting from including an additional normal distribution of activation energy for dynamics with average = 600 K and standard deviation = 120 K. The frequency dependent behavior qualitatively explains the observed in Fig. 4.4. The simulation result indicates that an inhomogeneity in activation energy can lead to the frequency dependency.

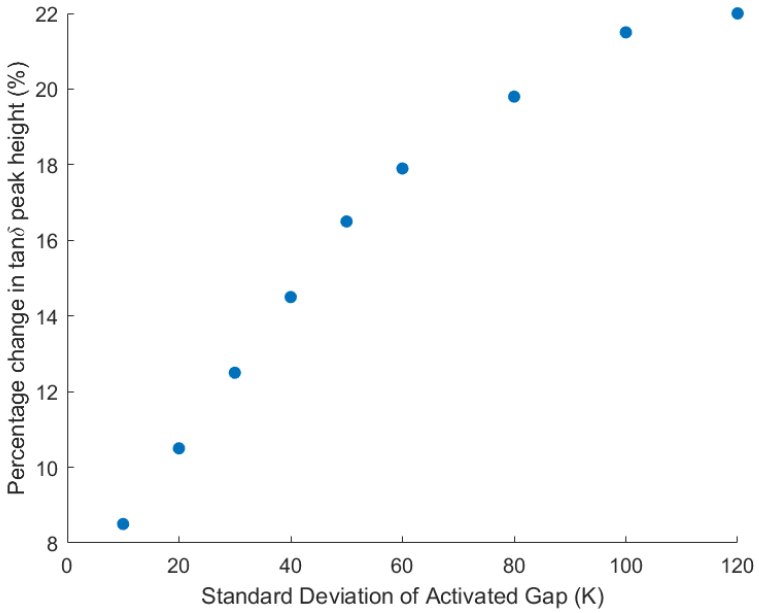

Figure 4.7: Simulated percentage difference in loss peak height comparing the case of 300 Hz and 10 kHz, as a function of standard deviation of the assumed normal distribution in activation energy incorporated into the simple Debye model. The distribution can account for up to a roughly 22 % difference.

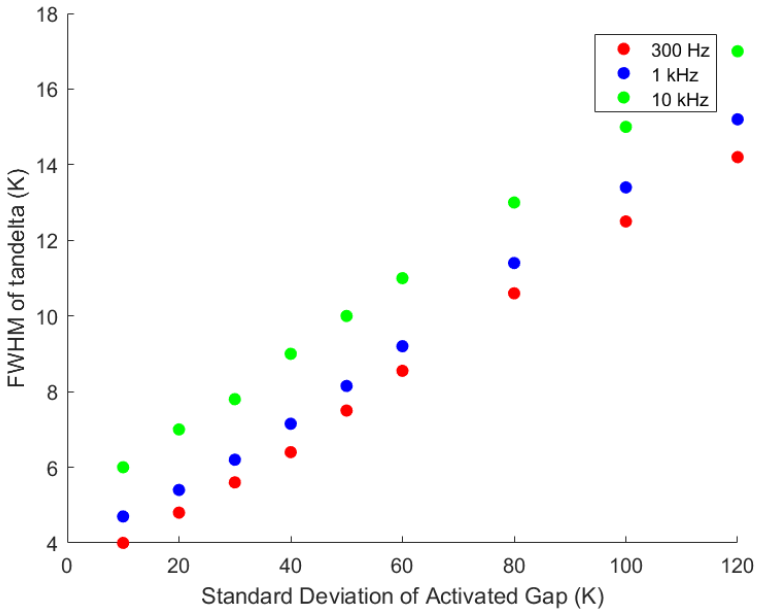

Figure 4.8: Simulated FWHM of the tanδ peak as a function of the standard deviation of the assumed distribution in activation energy that is incorporated into a simple Debye model, at the three measurement frequencies: 300 Hz, 1 kHz, 10 kHz.

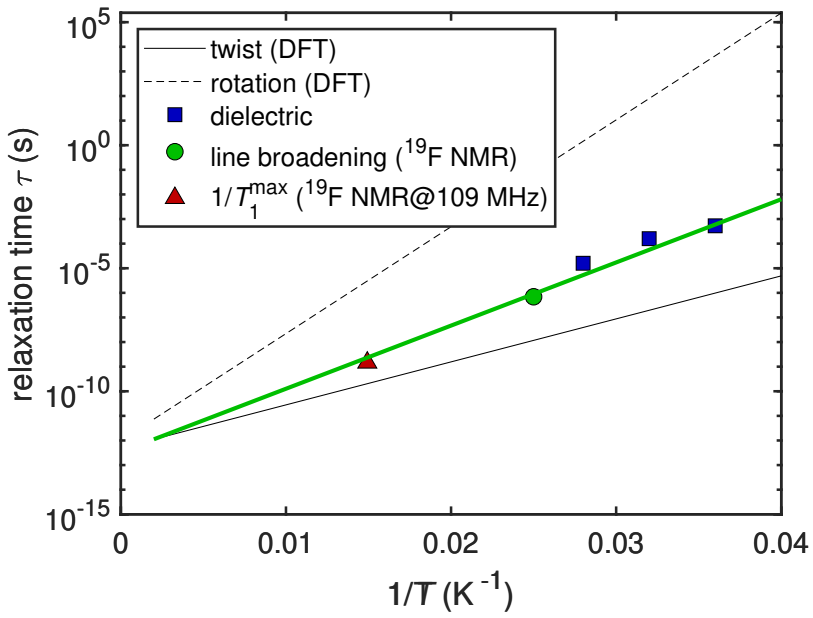

Figure 4.9: Comparison of the time scales from DFT calculations, NMR linewidth and spin-relaxation rate, and dielectric measurements. The solid black positively sloped line is based on DFT twisting motion (0.8 kcal/mole potential depth). The bold green line is plotted with the activation energy for the DFT twist multiplied by a factor of 1.5.

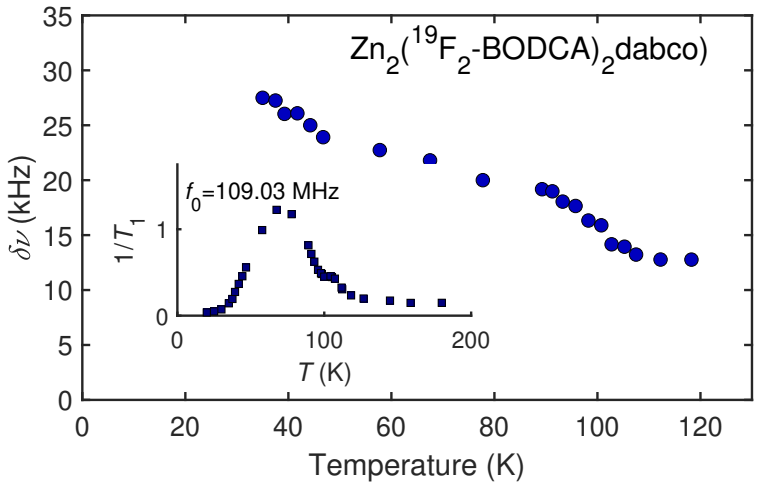

Figure 4.10: Temperature dependence of NMR linewidth FWHM $^{19}\delta\nu(T)$. Increases are observed in two independent temperature ranges, $T \lesssim 100$ K, and $T \lesssim 40$ K, which are attributed to phase transition and freezing of the rotators respectively. Line broadening is expected to occur at a crossover where time scale of the dynamics is of the order of $\delta\nu$. The inset is the ^{19}F NMR spin-lattice relaxation time as a function of temperature at the same magnetic field.

leveling off below about 90 K. Another onset of line broadening sets in on cooling below approximately T=40 K, below which $^{19}\delta\nu = 27.50$ kHz. We associate the two increases in linewidth with the phase transition, and the dynamical crossover. In the second case, the broadening is expected as the characteristic time scale slows down to be of order of the observed linewidth. Thus, the solid green circle in Fig. 4.9 corresponds to $^{19}\delta\nu = 27.50$ kHz, and $T = 40$ K. Additional dynamical information was gleaned from a peak in the spin-lattice relaxation rate, modeled using the standard Bloembergen-Pound-Purcell (BPP) analysis. The associated characteristic relaxation time is also included in Fig. 4.9.

4.2.2.1 NMR Measurement Details

The NMR spectrometer and the probe were built at UCLA, and a commercial superconducting magnet were set at magnetic field strengths $H_0 = 2.7217$ Tesla, with corresponding ^{19}F

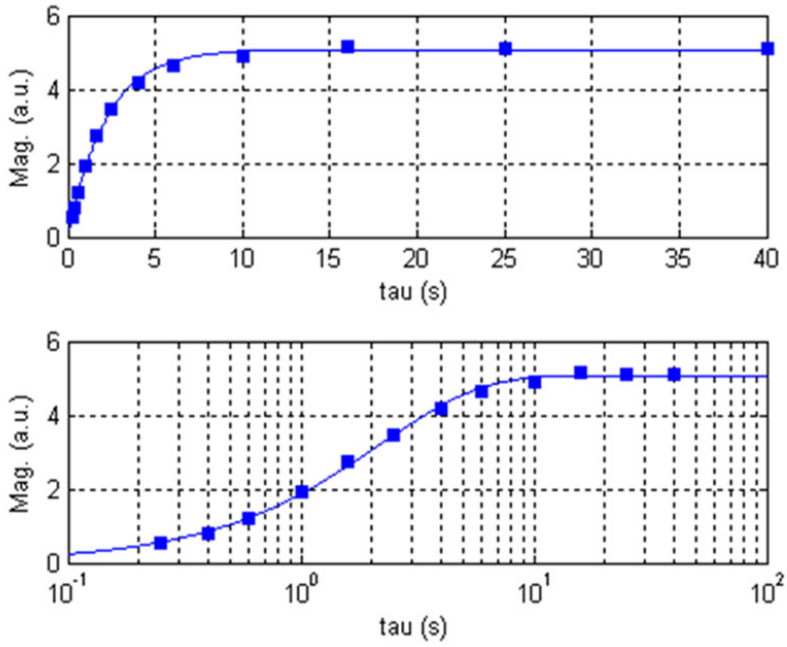

Figure 4.11: A representative example of a ^{19}F spin lattice relaxation experiment recorded at 44.25 K on the $Zn_2(F_2BODCA)_2$(dabco-H_{12}) sample, at 109.030 MHz utilizing a solid echo pulse sequence. The recovery times (tau) for the measurements were 250 ms, 400 ms, 600 ms, 1 s, 1.6 s, 2.5 s, 4 s, 6 s, 10 s, 16 s, 25 s, and 40 s. The integrated data were simulated as a single exponential recovery curve and the derived spin lattice relaxation time is 2.1931 s.

frequency 109.030 MHz. The powder sample was sealed in a tube with ultra-high Helium gas. An LC tank circuit was prepared in order for proper impedance matching and resonance conditions, where the sample being measured was placed in the inductor coil made of copper. ^{19}F T_1 experiments were executed by employing saturation recovery and solid-echo sequence. The nuclear spins were saturated by a pulse comb $(4 * \pi/2)$ followed by an adjustable recovery time τ and signal acquiring pulse. The acquired Fast-Fourier-Transform spectra of different τ would therefore amount to a saturation recovery curve, which was then well simulated as a single exponential function. Pulse lengths were calibrated at different temperatures as necessary. A representative recovery curve is shown in Fig. 4.11, and representative fully-recovered ^{19}F spectrum in Fig. 4.12.

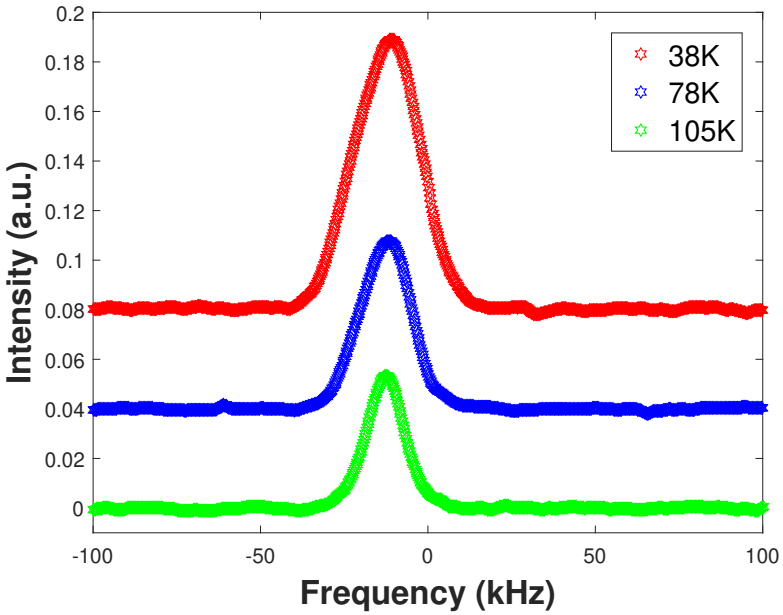

Figure 4.12: Three representative ^{19}F spectra are selected, including those taken at 38 K, 80 K, and 105 K, with carrier frequency being 109.03 MHz. The observed line-broadening, summarized in Fig. 4.10, is evident.

4.3 Simulation

4.3.1 Density Functional Theory Calculations

In order to identify the energy barrier corresponding to the activated relaxation, and otherwise to guide the analysis of the rotor interactions and dynamics, we carried out Density Functional Theory (DFT) [68] calculations of (F_2BODCA)-MOF motion. The calculated barriers for independent enantiomeric twisting and rotation are 0.8 kcal/mol and 2.0 kcal/mol, respectively, with uncertainty in the range of 0.2 to 0.4 kcal/mole [66]. The barrier for the coupled rotation-twist is calculated to be 1.4 kcal/mol. For the un-substituted BCO rotator [66], the two-fold symmetry of the stationary carboxylate groups and the three-fold symmetry of the rotator combine to give a six-fold symmetric rotator. The functionalized BODCA system breaks the symmetry and its associated coupled motion yields a potential with a point of interconversion between the two two-fold wells associated for each D_3^+ and D_3^- conformer. The lowest energy trajectory connects the two minima diagonal to each other and explores the D_3^+, D_3h, and D_3^- structures as shown in Fig. 4.14a. While the two fold rotational potential accounts for the two orientations that determine the dynamics of order-disorder transition, dipole oscillations above and below the ab-plane enabled by the twisting process are proposed to account for the dielectric behavior and Debye freezing in the ordered phase. The temperature dependence of this process (0.8 kcal/mol) is indicated in Fig. 4.9 by the thin black line, with a slope that is reasonably close to the experimental one indicated by the green line.

4.3.1.1 DFT Calculation Details

Our calculations were executed on an isolated molecule containing the F_2BCO group linked to assumed lithium atoms to avoid repulsive interactions between the carboxylate ions and the electronegative fluorine atoms. To mimic the crystal lattice environment, the two carboxylate groups were constrained to be co-planar, namely in the *ac* plane or *bc* plane as indicated in Figs. 4.2,4.13. The calculations were carried out using the M06-2X/6–311+G(d,p) hybrid

functional method [72]. Starting from the optimized structure, potential energy surface calculations were performed by scanning rotational and enantiomeric twisting dihedral angles, as illustrated in Fig. 4.3. The rotational angle was defined as the one between the plane of the carboxylate groups (O-C1-C2) and plane constructed by (C1-C2-C3), whereas the twisting angle was between (C1-C2-H) and (C2-C1-F) planes. Twisting reduces the D_3h symmetry to D_3 symmetry and overall, the oscillations explore the twisted D_3^+ and D_3^- structures as indicated in Fig. 4.13. The energy minima are found to be in the twisted conformation (D_3^+ or D_3^-) with fluorine atoms positioned away from the plane of the carboxylate groups, namely pointing in the *ab* plane.

Frequency calculations for the ground state structure yielded one imaginary frequency corresponding to the partial rotation of one of the carboxylate groups. This imaginary frequency arises due to the in-plane constraint. As expected, the transition state (TS) conformation was found with one imaginary frequency. The structure has a close approach to an oxygen of a carboxylate and the fluorine ions of F_2BCO. The imaginary frequency corresponds to the twisting and rotation of F_2BCO, and the transition state involves the coupled motion of the system.

4.3.2 Monte Carlo Simulations

The consequences on the paraelectric-antiferroelectric phase transition of a similar, or greater energy scale for the rotor-lattice rotational potential, when compared to the near-neighbor electric dipole interactions, were explored using a classical Monte Carlo simulation. For simplicity, our model assumed uniform, point dipole moments arranged in a lattice of alternating a/b rotation axes and we take into account the contribution of nearest-neighbor (NN), and NN plus next-nearest-neighbor (NNN) electric dipole-dipole interactions. The rotational potential energy associated with rotor-lattice interaction was varied as well. see Fig. 4.18. The dipole moment for a single rotator was taken to be 1.8 Debye in the simulation. The MOF structure constrains the dipole polarization vector to rotations about the ligand bonding axis. If near-neighbor dipole-dipole interactions dominate, then the simulated ground

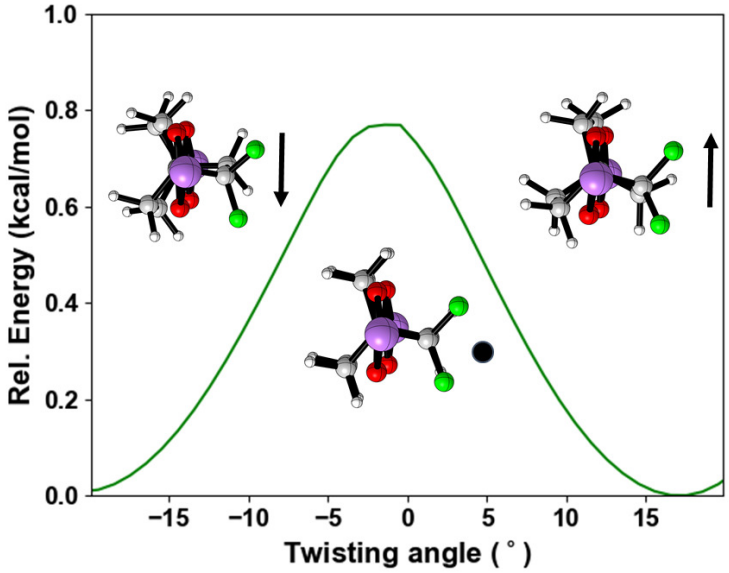

Figure 4.13: DFT energy scan of enantiomeric twisting as calculated using M06-2X/6-311+G(d,p) quantum mechanical method. The twist angle ranges from -20^o to +20^o, which would modulate the orientation and magnitude of the component of the dipole moment along the c-axis. The calculated potential energy barrier is 0.8 kcal/mol with a twisting attempt-to-escape frequency of 65.80 cm^{-1} ($1.97 \times 10^{12} s^{-1}$). These values indicate a twisting frequency of c.a. 10 kHz at 20 K, which is reasonably close to the temperature regime where the dielectric freeze-out behavior occurs. It is worthwhile to note that the 0.8 kcal/mol corresponds well to the activated behavior as simulated with the combined data of dielectric Debye-like freezeout and NMR linewidth shown in Fig. 4.9. [Figure courtesy of Ieva Liepuoniute.]

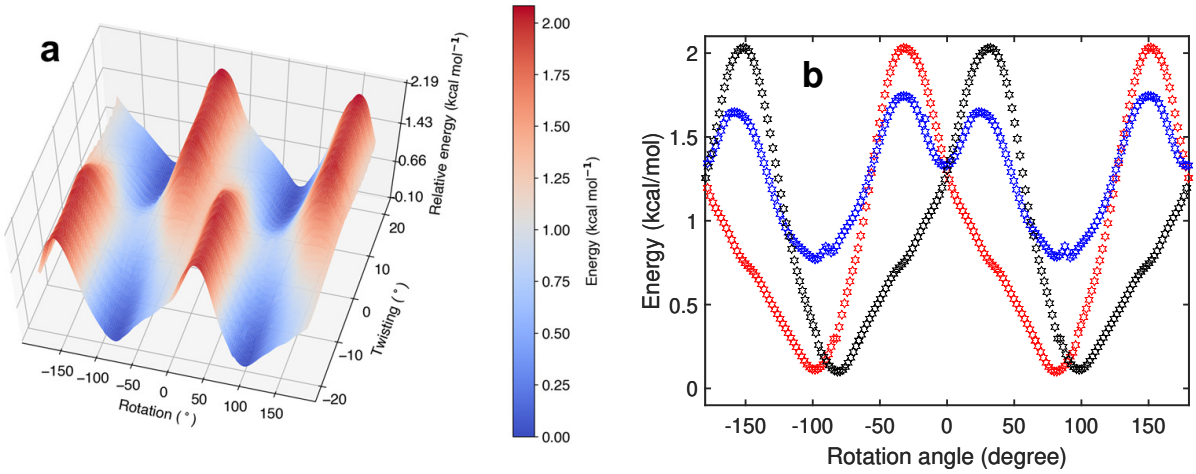

Figure 4.14: **a** DFT lattice potential energy landscape. The x- and y-axes indicate the rotational and enantiomeric twisting angles. **b** Cuts of the above DFT energy landscape at twist angles ca. + 20^o(red), - 20^o (black), and 0^o(blue) of the F_2BCO. The rotational angle ranges from -180^o to 180^o, and the calculated independent rotational energy barrier is ∼2.0 kcal/mol for -20^o and +20^o twist. The ground state conformation has fluorine atoms pointing away from the carboxylate oxygens. In particular, it is worthwhile to note that the coupling of the twisting and rotational degrees of freedom amounts to ∼1.4 kcal/mole lattice potential, which is lower than that of independent rotation. [Figure courtesy of Ieva Liepuoniute]

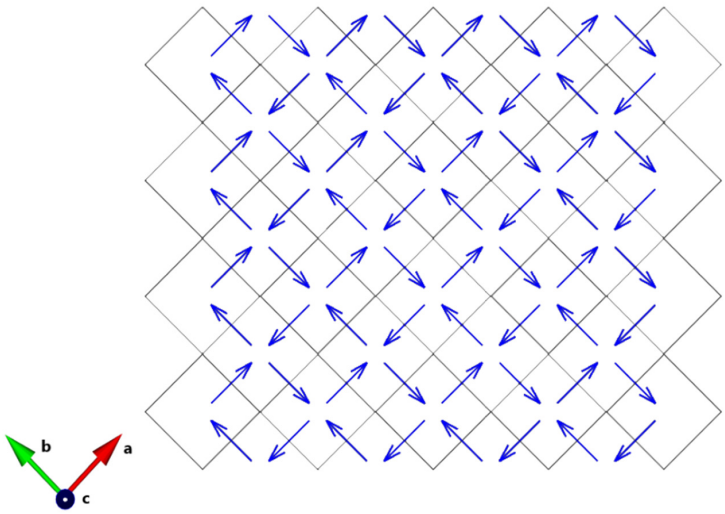

Figure 4.15: The simulated ground state of the spatial electric dipole configuration below the 100 K phase transition. The electric dipole moments all lie in the ab plane with alternating directions. If we decompose the dipole moments into two orthogonal components, they respectively form antiferroelectric configurations. The interaction under consideration is the electric dipole-dipole coupling among the first nearest neighbors and the second nearest neighbors. Each electric dipole moment is considered as 1.8 Debye.

state exhibits an ordered phase with dipole moments all lying in the *ab* plane, such that the underlying universality class is Ising. The ground state is shown in Fig. 4.18.

The sublattice polarization is shown as a function of temperature for various lattice potential amplitudes in Fig. 4.16. The general trend is a modestly increasing ordering temperature for the reduced thermally activated rotations resulting from increased lattice potential amplitudes. The overall normalization for the temperature corresponds to

$$k_B T_0 = \frac{p^2}{4\pi\epsilon_0 \langle d^3 \rangle}, \tag{4.7}$$

where k_B is Boltzmann constant, p is the rotor ligand dipole moment, ϵ_0 is vacuum permittivity, and d is the NN separation. For the range of strengths of relative lattice potential studied, quenched disorder does not significantly diminish the observed degree of ordering.

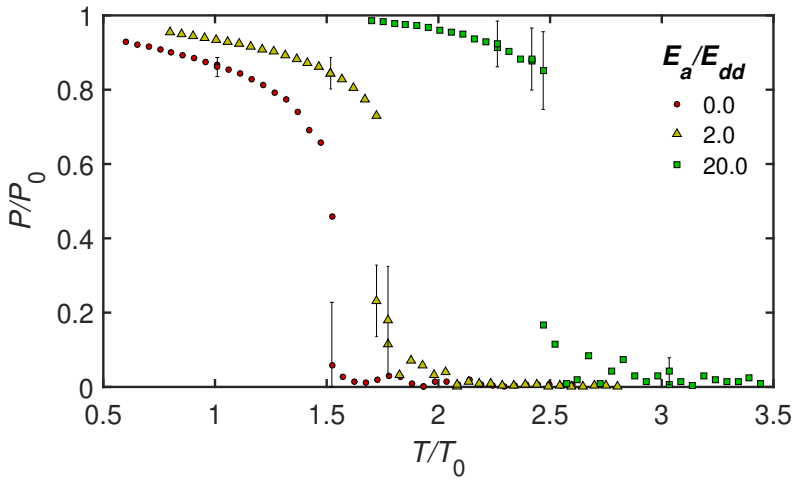

Figure 4.16: Temperature dependence of polarization of a sublattice given by Monte Carlo simulation, where the form of lattice potential input was assumed to be sinusoidal with 2-fold symmetry. Dipolar interaction and lattice potential with varied values as normalized to nearest-neighbor dipole-dipole interaction are taken into account.

4.3.2.1 Monte Carlo Simulation Details

Monte Carlo simulation was implemented using the Metropolis-Hastings algorithm [73, 74]. Of specific interest is the ground state, and the affect of applicable lattice potential amplitudes on the transition temperature T_c. For the range studied, T_c increased weakly, which is understood to be a consequence of the reduced fluctuations imposed by the increasing lattice potential. In the case of extremely large potentials, we presume that in the classical analysis carried out here, quenched disorder is expected to suppress the long range order.

Within a plane, the rotor sites are modeled as electric dipoles of fixed amplitude p and a single rotation axis. The integers i, j label the sites according to the arrangement shown in Fig. 4.17. The unit vector $\hat{u} = (u_x, u_y, u_z)$ defines a rotation axis; rotation by θ about $\hat{u}$ is defined by standard matrices [75]

$$R_u(\theta) = \begin{bmatrix} cos\theta + u_x^2(1-cos\theta) & u_x u_y(1-cos\theta) - u_z sin\theta & u_x u_z(1-cos\theta) + u_y sin\theta \\ u_y u_x(1-cos\theta) + u_z sin\theta & cos\theta + u_y^2(1-cos\theta) & u_y u_z(1-cos\theta) - u_x sin\theta \\ u_z u_x(1-cos\theta) - u_y sin\theta & u_z u_y(1-cos\theta) + u_x sin\theta & cos\theta + u_z^2(1-cos\theta) \end{bmatrix}.$$

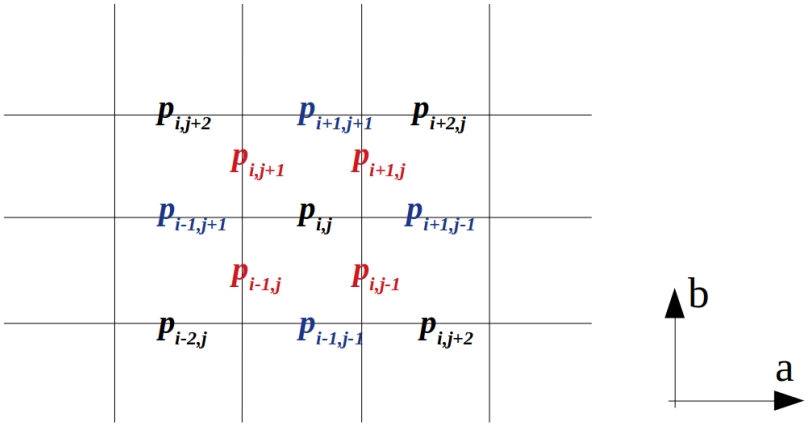

Figure 4.17: Depicted is the in-plane site labelling i, j used in the simulation. The red- and blue-coded are the nearest neighbors (NN) and the next-nearest-neighbors (NNN) of the dipole $\mathbf{p}_{ij}$ respectively.

Note that **a**-axis rotations correspond to $\hat{u} = (1, 0, 0)$, such that

$$R_a(\theta) = \begin{bmatrix} 1 & 0 & 0 \\ 0 & cos\theta & -sin\theta \\ 0 & sin\theta & cos\theta. \end{bmatrix}.$$

The rotors were initially confined to a strictly 2D square lattice. However the effect of interplanar coupling was also investigated. The initial state is chosen randomly. Monte Carlo steps follow the Metropolis-Hastings algorithm [73, 74], while assuming the system is in contact with a thermal bath at temperature T. The total interaction energy (between point dipole moments) is evaluated as

$$H = \sum -\frac{p^2}{4\pi\epsilon_0 r^3}(3(\mathbf{p}_{ij} \cdot \hat{r})(\mathbf{p}_{ij,neighbor} \cdot \hat{r}) - \mathbf{p}_{ij} \cdot \mathbf{p}_{ij,neighbor}) + U_{lattice}, \tag{4.8}$$

with r the distance between interacting dipoles and $U_{lattice} = \gamma \sin\theta$. Both NN ($r$=1.07 nm/$\sqrt{2}$)and NNN (1.07 nm) dipole-dipole interactions were investigated with no change in ground state and little change in transition temperature. The dipole-lattice potential $U_{lattice} = \gamma sin\theta$ was taken from the DFT results: γ= 2 kcal/mole and lowest-order 2-fold rotational symmetry favoring in-plane orientation of the dipole moment. The moment amplitude $p = 1.8$ Debye was set to that given by the AM1 method using Spartan software [16].

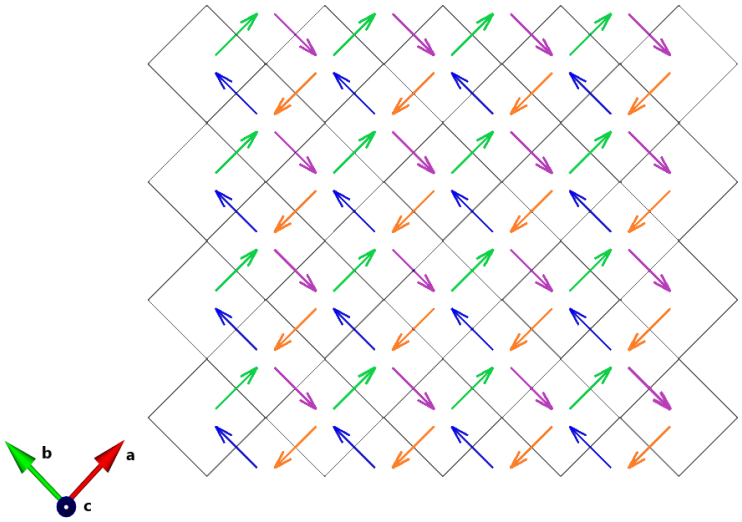

Figure 4.18: Illustrated is the simulated ground state. For the range $\gamma > 0$ studied here, T_c increases weakly whereas the ground state is unaffected.

Fig. 4.18 shows the ground state of spatial dipole configuration within the ab plane, where the moments all lie in the ab plane on 4 (interlocked) sublattices with polarizations P_k as defined in Eq. 4.9. The staggered polarization[76] for the entire lattice is taken as the order parameter, expressed here as $P = \sum_{k=0}^{3} e^{i\frac{\pi}{2}k} P_k$.

$$P_k = p|\sum_{sublattice} \hat{p}_{i,j}|, \tag{4.9}$$

normalized to the number of lattice sites and measurements taken. The results for P are shown in Fig. 4.19, which includes results for the strictly 2D case and both NN, NNN interactions (orange points). This is contrasted to a calculation corresponding to a bilayer and NN interlayer interactions. Since the interlayer interaction is not frustrated, a small increase in transition temperature is generically expected by including it. Here, no change is resolved, but this could be attributed to the small lattice size employed. Furthermore, as demonstrated in Fig.4.20, the planes of the ground state of this 3D case alternates in an anti-parallel fashion.

Finite size effects were also investigated [73]. Issues in this regard include the following. It will be more challenging to equilibrate a system with smaller lattice size due to its being away

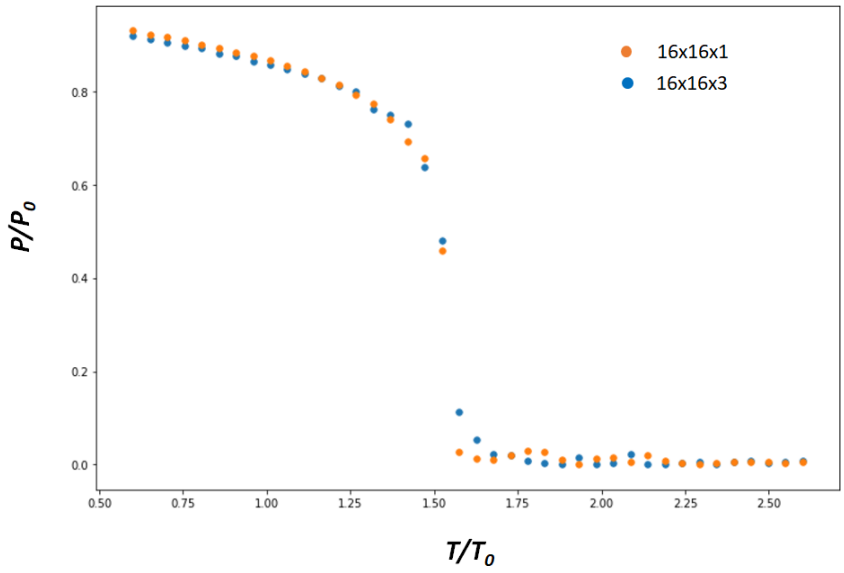

Figure 4.19: Sublattice polarization as a function of temperature contrasting the result for a monolayer (16 x 16 x 1, $\gamma = 0$) to that for a trilayer (16 x 16 x 3). Within the plane, NN and NNN interactions are included; out-of-plane includes NN coupling. The normalization is $k_B T_0 = \frac{p^2}{4\pi\epsilon_0 r^3}$, P_0 is the sublattice polarization of ground sate configuration.

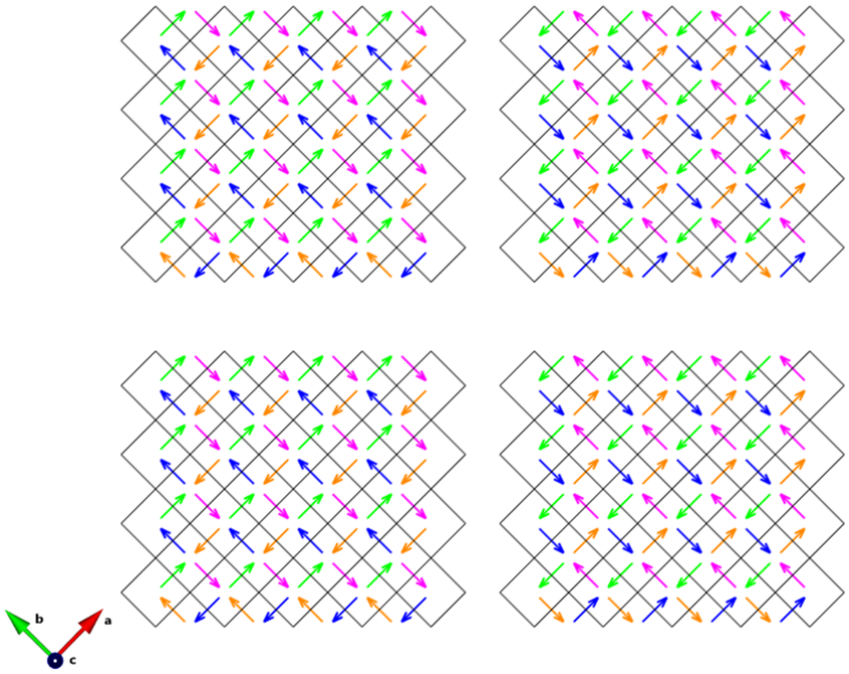

Figure 4.20: The ground state of the $8\times8\times4$ lattice. The 4 ab planes are stacked sequentially from upper left, upper right, lower left, to lower right. In addition to the 2 antiferroelectric patterns within the ab planes, it can be seen that the ab planes alternate in an anti-parallel fashion.

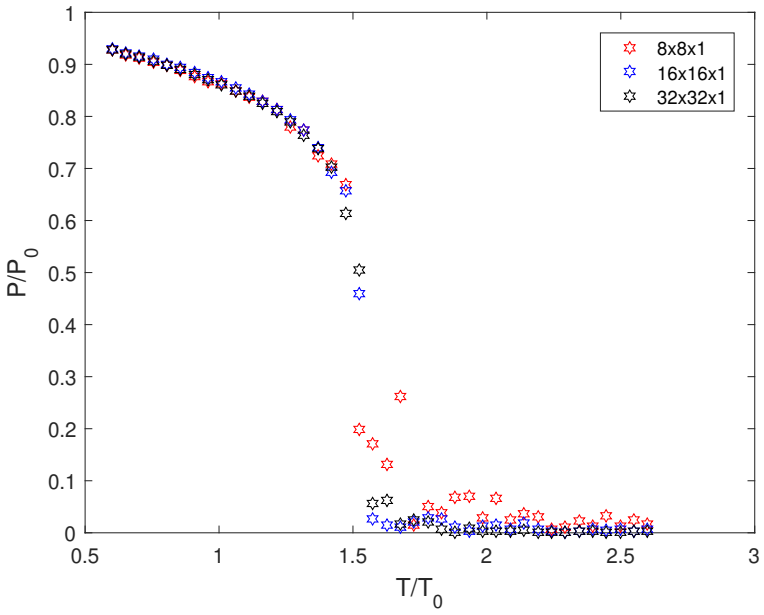

Figure 4.21: Finite size effect of the Monte Carlo simulation. The results indicate that the phase transition is reasonably defined for the calculation lattice sizes, which are sufficiently large.

from thermal equilibrium limit. Hence, the system is more susceptible to thermal fluctuation, which requires a larger number of averages to tackle uncorrelated noise. Fortunately in our case, with lattice size larger than $16 \times 16 \times 1$, this issue of noisy result can be reasonably suppressed, allowing for a decent designation of phase transition as can be seen in Fig. 4.21. Because, strictly speaking, the phase transition only occurs in the thermodynamic limit, less distinct is the corresponding phase transition of finite lattice size is expected and the size dependent polarization can be described by finite size scaling. For the 2D Ising ferromagnet, the finite size scaling of the order parameter, $M(T) \sim (Tc - T)^{\beta} \rightarrow L^{-\beta/\mu}$ where μ is crtical component relevant to the temperature dependent correlation length [73]. In our case, the lattice dimension of $16 \times 16 \times 1$ reasonably converges with that of $32 \times 32 \times 1$, indicating the finite size effect in this respect is insignificant when lattice size is larger than $16 \times 16 \times 1$. Below the second order phase transition temperature, finite sized lattice would encounter spontaneous-spin-flip of the entire lattice with probability inversely proportional to lattice size, and therefore, spatially, there coexist regimes that correspond to order parameter with phase difference $e^{i\pi}$, which would lead to cancellation of the resultant polarization [73, 77]. Solutions to this issue include taking root mean square order parameter [77] or taking absolute order parameter [73] before normalizing to the entire number of lattice sites. Here we adopt the latter approach. Although the solution would lead to finite polarization above the phase transition, it is considered inconsequential in terms of pinpointing the phase transition temperature. In addition, the polarization of the cases of $16 \times 16 \times 1$ and $32 \times 32 \times 1$ being sufficiently close to zero would indicate this trade-off can be reasonably be reasonably set aside.

4.4 Summary

Crystalline molecular rotors are a promising system for collective molecular machines since its correlated motion of the rotating molecules plays a pivotal role in realizing controllable machines responsive to external stimuli. The functionalized material system studied here, $Zn_2(F_2\text{-BODCA})_2(\text{dabco-}H_{12})$ molecular rotors, was fabricated and characterized by powder

X-ray diffraction, revealing its tetragonal lattice with alternating layers of polar rotors on the a-b plane and nonpolar rotors with axis parallel to c direction. Variable-temperature dielectric measurements unveiled two features, one corresponding to a phase transition at $T_c = 100$ K, and a second is associated with a dynamical crossover occurring at lower temperatures. The frequency dependency of this feature can be understood in the framework of the Debye relaxation model, with the additional consideration of a distribution in dynamic activation energy to account for the frequency dependent loss tangent maximum. The observed transition temperature corresponds well to the expected nearest neighbor dipole-dipole coupling strength. Monte Carlo simulations including nearest neighbor and next nearest neighbor couplings reveal an antiferroelectric ordering, also in the appropriate temperature range.

DFT calculation provided the conceptual framework in relation to the observed dynamical crossover. Namely, the lattice potential stiffness is controlled by a thermally activated internal twisting of the rotors. As the twisting is frozen out, the effective rotational motion is suppressed, with the affect of suppressing the dielectric response.

The results of our study indicate that the rotational potential energy barrier is sufficiently small that the dipole-dipole interaction drives an antiferroelectric phase transition. Our work suggests that fluorine-grafted crystalline molecular rotors bearing correlated behaviors is an auspicious material platform to be utilized as a responsive machine component on the nanoscale in the foreseeable future.

While we are improving our understanding of the overall physics of the material $Zn_2(F_2$-BODCA$)_2$(dabco-H_{12}), the detailed structural and dipole ordering have not yet been corroborated by further evidence. In this regard, prudent investigation of the structure of the material as a function of temperature would be conducive. Predicated on the sound structural data, theoretical simulation taking into account the coupling of intraplane neighboring dipolar rotors and the inter-plane coupling has assisted in explaining the ordering as a consequence of the competition between dipolar energy and thermal energy.

For many years, scientists have been working toward realizing functional nanoscale machines. The significance was highlighted by the awarding of the 2016 Nobel Prize in Chem-

istry. Molecular rotors serve as a relatively unexplored platform. For dipolar molecular rotors, there are several tunable parameters, such as the arrangement of the framework (crystal structure), the free space available, the extent of correlated motion between the rotating molecules and its surrounding framework, the symmetry, size, and spatial configuration of the rotating dipolar molecules, the distance between adjacent rotating dipolar molecules, and the strength of the individual permanent electric dipole moments.

CHAPTER 5

Correlated Electronic System

5.1 Introduction

The focus of our research is to observe oxygen-17 NMR Knight shift[1] as a function of temperature on cooling through the superconducting critical temperature T_c, in the presence of variable strain. The uniaxial strain is achieved by utilizing a piezoelectrically driven actuator [3]. Fig. 5.2 shows the setup of the strain cell with the sample and NMR coil mounted on top. Oxygen-17 NMR is sensitive to the spin polarization M_s. If the system is a s-wave (singlet) superconductor, the shift $K \to 0$ in the limit of low temperature ($T/T_c \to 0$) and magnetic field strength ($B_0/B_{c2} \to 0$). Here, T is the temperature in Kelvin, B_0 is the static magnetic field and B_{c2} is the upper critical field. On the other hand, the expectation for the widely considered E_u state, as listed in Table 5.1, is that the shift remains constant from normal-state to superconducting state. Summarizing, the results indicate that when cooling down below critical temperature, the Knight shift decreases for all strains applied, inclusive of zero strain, in disagreement with previous reports [5]. We thereby implemented a series of tests to understand the discrepancy, which we believe is due to heating effect caused by NMR pulses.

The crystal structure of Sr_2RuO_4 is shown in Fig. 5.3 and is identical to that of copper oxides, La_2CuO_4. The O(2) sites are in the apical positions, symmetrically above and below the Ru site. In this work, the static magnetic field B_0 is applied parallel to b direction because out-of-plane field components suppress B_{c2}, which would render the window to

[1]The general expression for Knight shift is: $K_s = A\chi$ where A is the hyperfine coupling constant and χ is spin susceptibility.

Table 1 | Irreducible representations for selected allowed *p*- and *d*-wave order parameters compatible with the D_{4h} symmetry of Sr_2RuO_4

Representation	Basis function	Nodes	TRSB	χ_{b0}/χ_N
A_{1u}	$\mathbf{d}=\hat{\mathbf{x}}k_x+\hat{\mathbf{y}}k_y$	No	No	1/2
B_{1u}	$\mathbf{d}=\hat{\mathbf{x}}k_x-\hat{\mathbf{y}}k_y$	No	No	1/2
A_{2u}	$\mathbf{d}=\hat{\mathbf{x}}k_y-\hat{\mathbf{y}}k_x$	No	No	1/2
B_{2u}	$\mathbf{d}=\hat{\mathbf{x}}k_y+\hat{\mathbf{y}}k_x$	No	No	1/2
B_{1g}	$\psi_d=k_x^2-k_y^2$	Vertical	No	0
B_{2g}	$\psi_d=k_xk_y$	Vertical	No	0
E_u	$\mathbf{d}=\hat{\mathbf{z}}(k_x\pm ik_y)$	No	Yes	1
E_u	$\mathbf{d}=k_z(\hat{\mathbf{x}}\pm i\hat{\mathbf{y}})$	Horizontal	Yes	1/2
E_g	$\psi_{\text{chiral}}=k_z(k_x\pm ik_y)$	Horizontal	Yes	0

Figure 5.1: Possible order parameters for the superconducting state of Sr_2RuO_4. χ_{b0} is the ground state susceptibilities with B_0 parallel to b axis. χ_N is the spin susceptibility of the normal state. Spin orbit coupling effect is neglected here.

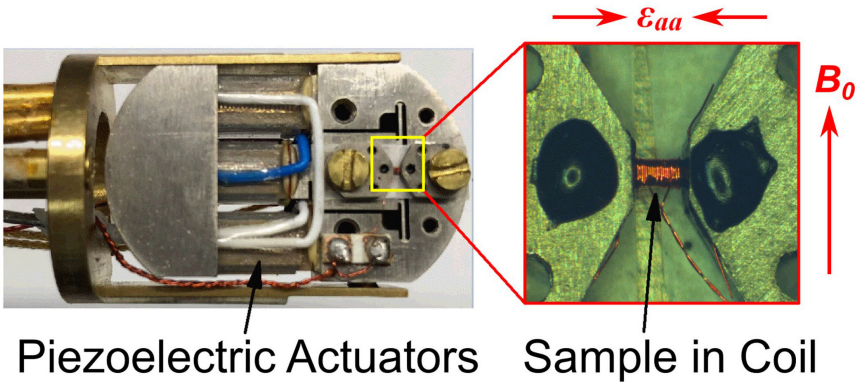

Figure 5.2: The strain cell (Razorbill 120) with the mounted sample. The strain cell and sample are oriented such that uniaxial strain is along $\boldsymbol{a}$ direction and static magnetic field is along $\boldsymbol{b}$ direction. The NMR Cu coil is winded around the sample portion that is not glued, which is roughly 0.9 mm long and is the part to be strained.

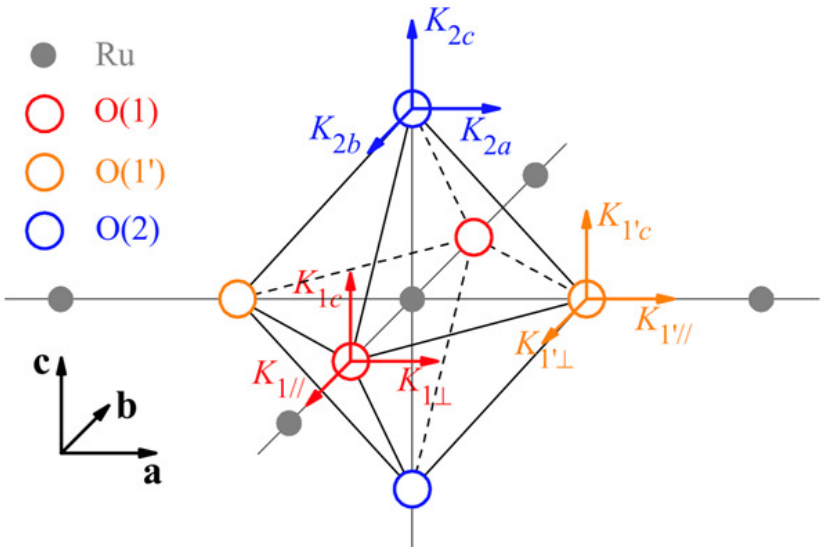

Figure 5.3: The crystal structure of Sr_2RuO_4. Uniaxial stress is applied along the $\boldsymbol{a}$ direction, and static magnetic field is along the $\boldsymbol{b}$ direction. Knight shifts are measured for the in-plane O(1) and O(1') sites.

observe superconductivity smaller. Uniaxial strain ϵ_{aa} is applied along the a direction. The states at E_F are derived from hybridization of Ru t_{2g} and O π orbitals, as shown in Fig. 5.5.

Restricting the field strength to small values minimizes field-induced quasi-particles (which can overwhelm the response of the superconducting state), the applied static magnetic field needs to be much smaller than upper critical field to avoid quasi-particle spin polarization. On the other hand, the NMR signal strength increases in larger magnetic fields[2]. The optimal situation is to maximize upper critical field. As shown in Fig. 5.4, the upper critical field reaches the maximum value of 4.3 Tesla and so does critical temperature.

[2]Nuclear spin polarization prefers large field leading to large population inversion.

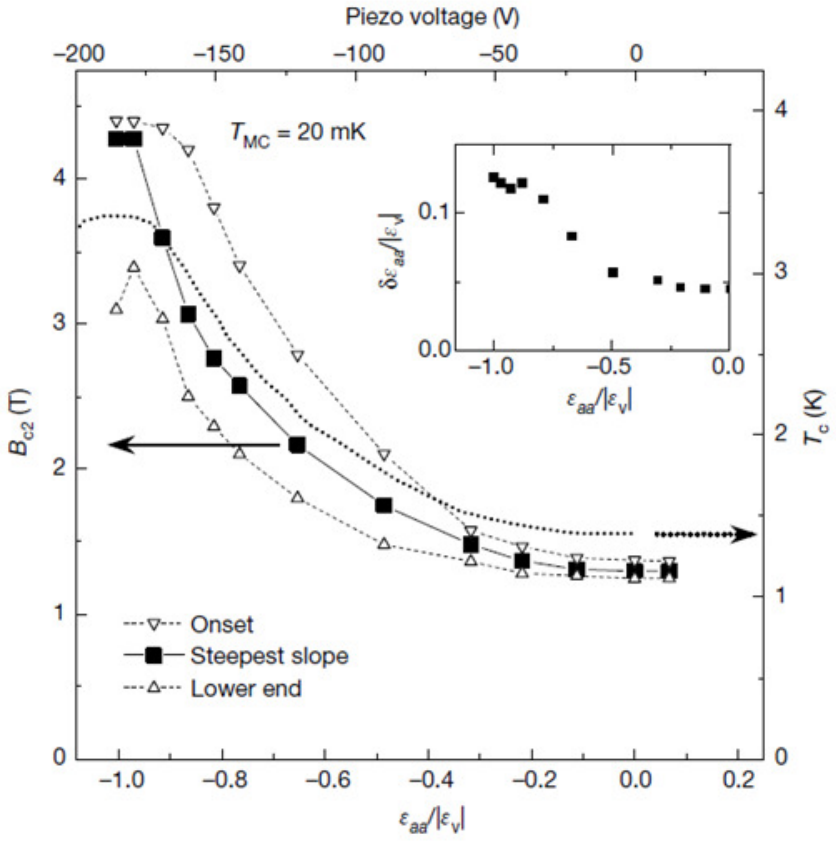

Figure 5.4: Upper critical field and transition temperature as a function of uniaxial strain along a axis. At T = 20 mK, we determine the upper critical field by implementing a.c. susceptibility measurements as a function of uniaxial compressive strain ϵ_{aa}. The trend of B_{c2} corresponds well to that of transition temperature T_c [4]. The inset is strain gradient δ_{aa}, which increases with higher compressive strain.

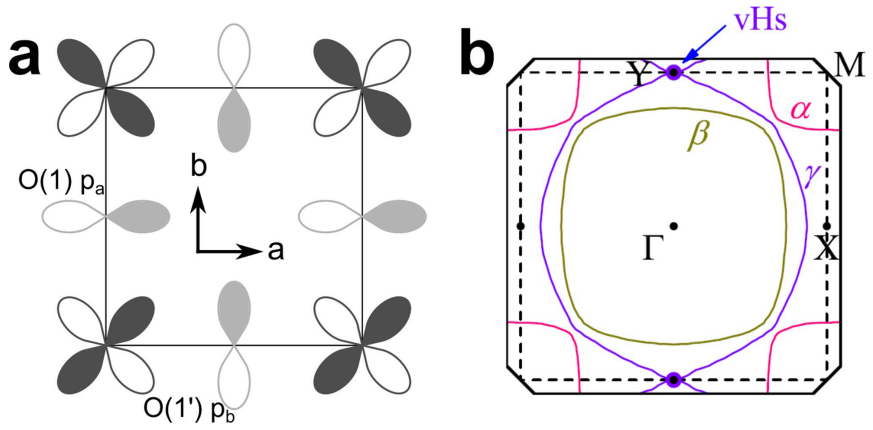

Figure 5.5: a. Ru d_{xy}-orbital and O p-orbital hybridizing on the RuO_2 plane corresponding to the Y point in b. O(1) and O(1') are the sites where Knight shifts are measured. b. The configuration of band structure at Fermi level. Compression along a direction ($\epsilon_{aa} < 0$) forces the γ band distorted toward the Y point on the Brillouin zone boundary, leading to van Hove singularity in the density of state on the Fermi surface when γ band touches boundary.

5.2 Experimental

5.2.1 Crystal Structure

The crystal structure of the material is shown in Fig. 5.3. Oxygen ions are at the corners and Ru ions at the center of each octahedron. Fig. 5.5a shows the hybridization of Ru and O orbitals that dictate the characteristics of γ band at Y point[3] at Brillouin zone boundary. The oxygen ions in the ab plane were originally equivalent, but with the application of static magnetic field B_0 in the b direction they become distinguished and are labelled O(1) and O(1') sites respectively with distinct Knight shifts. Applying the uniaxial strain ϵ_{aa} in the a direction forces the Y point at Fermi level of γ band toward Brillouin zone boundary amounting to a peak in density of state at Fermi level, coined van Hove singularity [43].

[3]Y is the location where the Fermi surface of the γ band passes through the BZ boundary, leading to a Fermi surface reconstruction that is called a Lifshitz transition. The effect is a consequence of the compressive uniaxial strain, which distorts the Fermi surface.

5.2.2 Materials Processing

The floating-zone method [32] is utilized to prepare the high quality single crystal Sr_2RuO_4. Samples were cut and polished along the a,b,c axis with dimension on the order of $3\times0.3\times0.15$ mm^3, with 3 mm defined as the a axis. The as-prepared material is annealed in 50% oxygen-17 enriched oxygen atmosphere at 1323 K for two weeks. The oxygen-17 enrichment does not change critical temperature [43].

5.2.3 Stain Cell Setup

Uniaxial stress was applied by expanding and contracting the piezoelectric stacks on the Razorbill strain device. The sample was clamped and glued between two plates on each side with black Stycast 2850 (Loctite). The portion that is strained uniaxially has the length of 0.9 mm. Compression or extension of the sample along the a axis is measured by an accompanying parallel plate capacitor. The middle (unglued) part of the sample is winded with 25-μm Cu wire of roughly 23 turns. As shown in Fig. 5.2, ϵ_{aa} is parallel to a axis and B_0 is parallel to b axis.

5.2.4 NMR Measurements

Spin echo was utilized for the NMR measurements, with the strain ϵ_{aa} parallel to a axis and the applied static magnetic field B_0 parallel to b axis. Two samples, S1 and S2, were investigated. For S1, it was compressed to a critical point with critical temperature = 3.5 K[4]. The carrier frequency = 11.54 MHz and static field = 1.9980 Tesla. Temperature was varied in the neighborhood that covers the critical point. For S2, two sets of measurements were carried out. For two temperatures of 20 mK and 4.3 K, strain was varied from zero to -0.58%, with carrier frequency fixed as 6.7 MHz and static field at 1.1573 Tesla. With carrier frequency fixed at 4.137 MHz and static field at 0.7107 Tesla, temperature was kept

[4]When the uniaxial stress is applied, essentially the Fermi energy is tuned. Fermi surface reconstruction occurs at a Lifshitz transition.

at 20 mK, measurements were carried out as a function of strains. For S2, all measurements were aided by a dilution refrigerator (Oxford Kelvinox). The strain cell, tank circuit, and the sample were all immersed in the mixing chamber. The strength of the static field is determined by the ^{3}He spectrum at the applied carrier frequency. Temperature calibration is based on T_1 measurement of ^{63}Cu of the coil with the tabulated relationship $T_1T = 1.27$ s K.

5.3 Knight Shift as a Proxy

Fig. 5.6 is the oxygen-17 NMR spectra taken at various temperatures and at van Hove singularity with B_0 =1.9980 Tesla. One can see the evident Knight shift change as a function of decreasing temperature crossing critical point. Due to small orbital shifts, when the Knight shift is zero, the frequencies are primarily affected by quadrupolar effects [43].

Due to the presence of field-induced quasi-particles, the spin polarization may increase nonlinearly with field strength. Thus, in the superconducting state, we write the shift as

$$K \propto \frac{M_s}{B_0}, \tag{5.1}$$

and the Knight shift for the normal state has the characteristics $K_{1b} < 0, K_{1'b} > 0$. The changes in Knight shift when temperature is lowered below T_c in Fig. 5.6b indicate a decrease of M_s by 20–30%, which is qualitatively different than the results previously reported [5]. It should be noted that the Knight shifts remain finite in the case that $B_0 \neq 0$ and in the limit $T \to 0$. As stated above, the source for the response can be predominantly that of field-induced quasi-particles. Due to the new result, obtained under strained conditions, we were motivated to follow the magnetic response on lowering the strain. On doing so, we found a similar reduction of K under unstrained conditions. The observations were properly obtained only after investigating the role of heating by the RF pulses. We concluded that the standard measurements warmed the sample to temperatures greater than the critical temperature $T_c(B_0)$. That is, the recorded NMR transients were improperly measurements of the normal state spectrum.

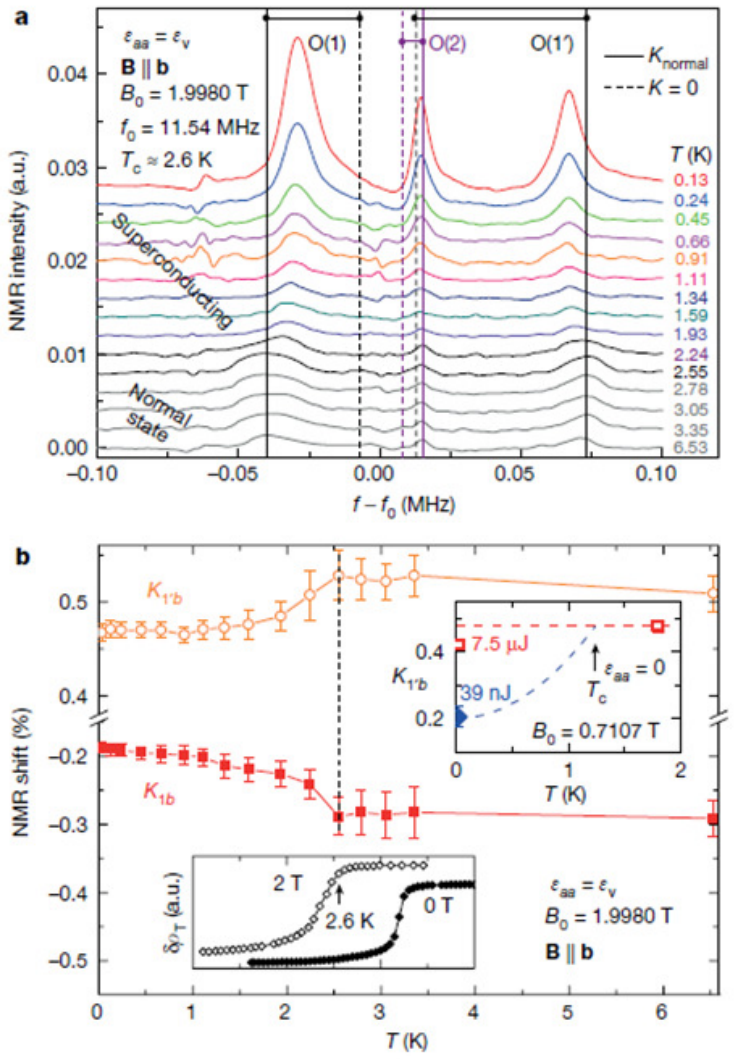

Figure 5.6: With compressive strain ϵ_{aa} at roughly 0.7%, the Knight shift as a function of temperature is recorded. a. The NMR experiments were carried out with the static magnetic field $B_0 = 1.9980$ Tesla and the carrier frequency $f_0 = 11.54$ MHz. The solid vertical lines correspond to normal state positions, whereas the dashed lines represent zero Knight shift positions. b. Evident reduction in the associated Knight shifts is observed below $T_c(B_0) = 2.6$ K. In the lower inset, δ_{ρ_T} denotes the change of the reflection coefficient, indicating the transition between normal state and superconducting state. The reduction is corresponding to drop in spin polarization M_s in the superconducting state. In the upper inset, Knight shift as a function of pulse energy presents a similar decrease of M_s below T_c for $\epsilon_{aa} = 0$ (see Fig. 5.7 for details).

5.4 Contingency on Pulse Energy

With the static field magnetic field $B_0 = 0.7107$ Tesla (similar to the 0.65 Tesla in [5]), and mixing chamber temperature T=20 mK, we mapped out the oxygen-17 spectra as a function of pulse energy. $B_0/B_{c2} \simeq 0.55$, and strain $\epsilon_{aa} = 0$. As shown in Fig. 5.7, the three main peaks are the central transitions of O(1), O(2) and O(1′), from low to high frequency. The top spectrum of Fig. 5.7a is taken at T = 1.8 K using a spin echo sequence, and serves as the normal state reference. The other spectra were recorded at T = 20 mK, using a single pulse with varied pulse length corresponding to different transmitted energies. The Knight shift as a function of transmitted energy is shown in Fig. 5.7b.

To better understand the possible heating effect resulting from applied pulses, time-resolved measurements of the reflected power from the tank circuit were implemented. An excitation pulse is applied, followed by the application of lower-power continuous wave. The time-dependent reflected wave of the CW was detected in quadrature, and time-synchronous with the initial excitation pulse. The sample is unstrained in this case. The reflected power is tracked as a function of time, which should be contingent on the response of the sample to input pulse. The measurement is equivalent to an a.c. susceptibility and is related to radio-frequency shielding. As shown in Fig. 5.8, for pulse energy larger than 9.4 μJ, the recovery to a steady state is a two-step process, which we interpret as an indication of an initial warming to the normal state, followed by a slower process involving vortex dynamics.

5.5 Summary

In summary, the main finding of our work is that for all uniaxial strain applied, including the zero strain case, the Knight shift, and therefore the spin polarization[5] is reduced in the superconducting state, relative to that of the normal state. The result does not support any odd-parity order parameter with an out-of-plane $\boldsymbol{d}$ and provides constraints on the orders

[5] A reduced spin polarization leads to a reduced Knight shift, not reciprocally.

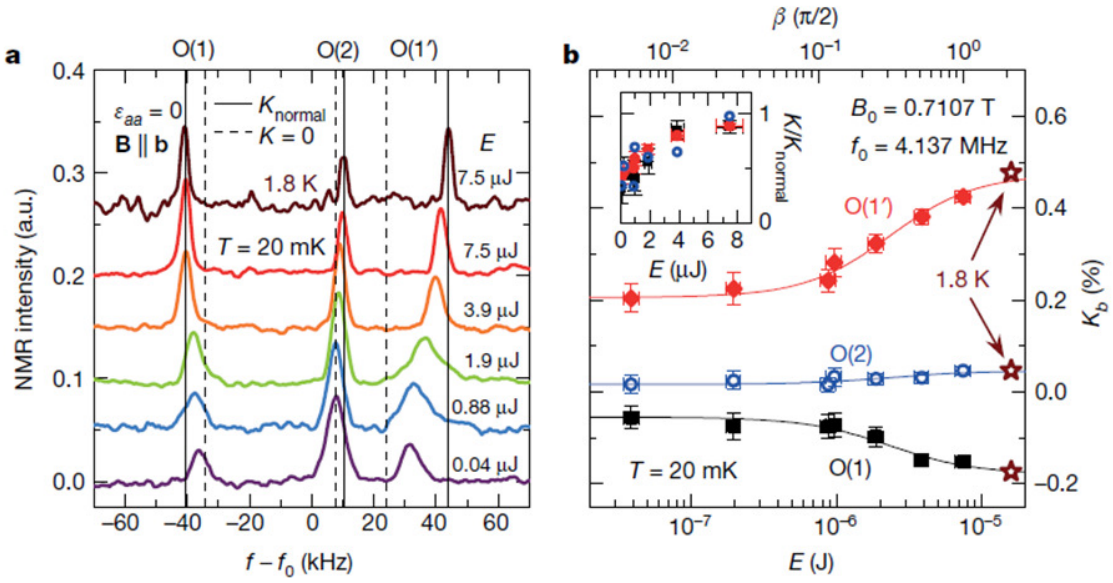

Figure 5.7: Without uniaxial strain applied, ^{17}O NMR spectra of Sr_2RuO_4 is recorded as a function of pulse energy. a. Free induction decay measurements were implemented as a function of pulse length d_1, which is set to be smaller than $d_{\pi/2}$. $\pi/2$ corresponds to 7.5 μJ in energy. Measurements were implemented at nominal base temperature 20 mK, static magnetic field $B_0 = 0.7107$ Tesla and $f_0 = 4.137$ MHz. In the left figure, solid vertical lines represent normal state position while the dashed lines indicate the position without any Knight shift. b. NMR Knigt shift as a function of applied pulse energy, which can be translated to tip angle β . Inset is the change of Knight shift as referenced to that of normal state, which indicates comparable trend for the three oxygen sites.

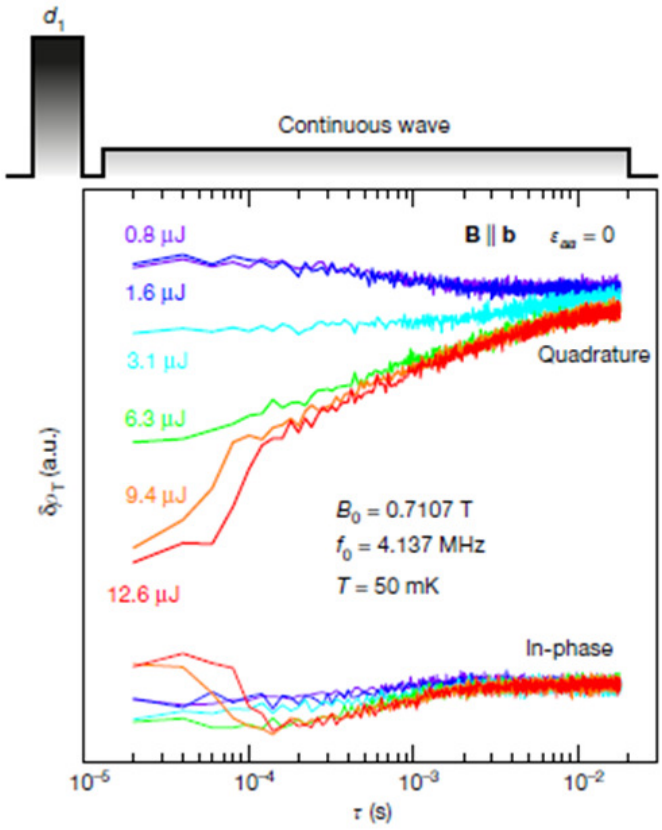

Figure 5.8: At $\epsilon_{aa} = 0$, and with the superconducting state as the initial condition, a pulse with varied energies is applied at time $\tau = 0$, which is immediately followed by a low-power time-resolved continuous wave (CW) measurement of the phase-sensitive NMR power reflected from the tank circuit (a radiofrequency equivalent to a complex a.c. susceptibility measurement). Both the in-phase and quadrature parts of δ_{ρ_T} are strongly impacted at the beginning of CW reflection measurement, particularly for larger pulse energies. No similar transient effect is observed when the sample is initially in the normal state.

parameters that are still otherwise viable for Sr_2RuO_4. For other possibilities, listed in Table 5.1, one revealing signature is the magnitude of the change in Knight shift.

To further narrow down possible order parameters, a challenge is ascertaining the quasiparticle contribution in nonzero fields, which prevents us from discriminating between odd-parity order parameters ($A_{1,2u}$, $B_{1,2u}$ as listed in Table 5.1) and even-parity states. Nevertheless, the measurements carried out at the critical strain are inconsistent with all odd-parity states, which is at odds with $A_{1,2u}$, $B_{1,2u}$ and in contradiction to all triplet cases. At zero strain, the results are less constraining because the field strength was greater in comparison to B_{c2}. A solution to this difficulty is a larger sample volume, and higher ^{17}O concentration.

In the case where A_{1u} and B_{1u} may have identical critical temperatures, possible scenario is the formation of domains featuring either A_{1u} or B_{1u} with domain walls linked with time-reversal-symmetry-breaking. Domain formation should be manifested as a splitting or change in line shape since NMR is a probe sensitive to local environment. Nonetheless, no related signature is found in our result. For even-parity in-plane order parameters, $d_{x^2-y^2}$ and d_{xy} can not have identical critical temperature due to the crystal field being tetragonal. As such, the remaining possible order parameter with time-reversal-symmetry breaking would be $d_{xz} \pm id_{yz}$, corresponding to ψ_{chiral} in Table 5.1.

CHAPTER 6

Appendices

6.1 Synthesis of Crystalline Rotors

2,2-Difluorobicyclo[2.2.2]octane-1,4-dicarboxylic acid (F_2-BODCA) was prepared by deoxofluorination of the diethyl 2-oxobicyclo[2.2.2]octane-1,4-dicarboxylate diester. The reaction of F_2-BODCA with dabco and $Zn(NO_3)_2 \cdot 6H_2O$ in dry dimethylformadide (DMF) at 120^{o}C afforded the pillared MOF Zn2(F_2-BODCA)$_2$(dabco). The as-synthesized material was activated at 200^{o}C for 2.5 h. Single crystals of Zn_2(F_2-BODCA)$_2$(dabco) were obtained after activation, and the diffraction study was made at 100 K. The crystal structure of Zn_2(F_2-BODCA)$_2$(dabco) was solved in the tetragonal space group P-4 with a weighted R-factor of 0.1114 (Fig. 4.3a). The structure consists of a 2D-squared grid formed by dicarboxylate ligands and zinc paddle wheel clusters ([Zn_2(F_2-BODCA)$_2$]), which coordinate to dabco in the orthogonal direction to complete the 3D structure. Additionally, the structure shows that both the dabco pillar and F_2-BODCA rotator are disordered. As the three-fold symmetric dabco spacers sit in a crystallographic center of symmetry, they occupy, on average, two positions related by a 60° rotation with equal probability. The F_2-BODCA rotator is positionally disordered with both sides of the structure occupied by the terminal F-atoms, also with equal probability. Although F_2-BODCA is in a general position, rotational disorder is manifested in the diffraction study by the distribution of the F atom electron density attached to several of the disordered carbon sites across the periphery of the F_2-BODCA cage.

Cross polarization and magic angle spinning (CP-MAS) ^{13}C NMR experiments confirmed the general features of the structure with a number of signals consistent with the time-average

symmetry of the ligands, including two carboxylates and one carbon signal at low field that displays scalar coupling with the bound fluorine atoms for the rotator. The activated material is thermally stable from room temperature to 300^{o}C, as demonstrated by thermal gravimetric analysis (TGA). The phase identity of the activated powder samples was confirmed by powder X-ray diffraction. The permanent porosity of $Zn_2(F_2$- BODCA)$_2$(dabco) was characterized by N_2 sorption at T=77 K, which followed a type I isotherm with a BET surface of 996 m^2 g^{-1}. [Courtesy of Professor Miguel Garcia-Garibay's group]

6.2 Correlation Time

The correlation function $G(t,\tau)$ is devised to delineate the random rotor motion in the sample concerned. It is defined as:

$$G(t,\tau) = \frac{1}{N}\sum_{i=1}^{N} B_{loc,i}(t)\cdot B_{loc,i}(t+\tau), \tag{6.1}$$

where $B_{loc,i}(t)$ is the local field experienced by spin i at a certain time t, and N is the total number of spins. If the molecule is spherical, then the correlation function takes on the form of

$$G(\tau) = G(0)\exp(-\frac{\tau}{\tau_c}), \tag{6.2}$$

where τ_c is the parameter that determines the speed of exponential decay.

J(ω,τ) is the Fourier transform of G(t,τ) and corresponds to the spectral density function.Spectral density takes on the following form [7]

$$J(\omega) = G(0)\frac{2\tau_c}{1+\omega^2\tau_c^2}, \tag{6.3}$$

where G(0) is contingent on strength of mean square local fields $\overline{\boldsymbol{B}_{loc}^2}$. An essential feature of $J(\omega)$ versus ω plot is that the area underneath the curve is constant because the number of rotating molecules are the same, irrespective of varying τ_c. This feature leads to an integral characteristic of $J(\omega_0)$ versus τ_c, in which $J(\omega_0)$ has its maximum value when $\omega\tau_c = 1$. It is worth mentioning that the characteristic of $J(\omega_0)$ directly determines that of spin-lattice

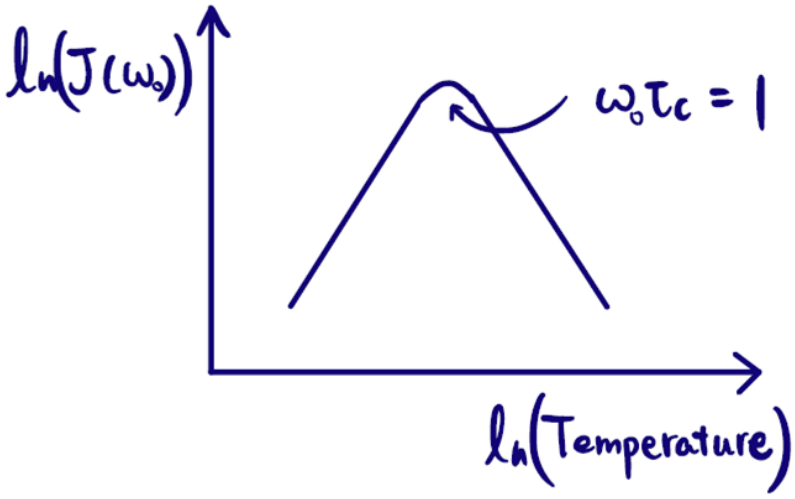

Figure 6.1: Spectral density $J(\omega_0)$ versus temperature. When $\omega\tau_c = 1$, the amount of molecules reorienting at Larmor frequency peaks, and as a result this is the condition where longitudinal relaxation, which is dependent on $J(\omega_0)$, is most efficient. Aside from the condition of $\omega\tau_c = 1$, there are two limiting scenarios. On one end, $\omega\tau_c << 1$ (high temperature regime) is the fast limit, where τ_c is fairly short; on the other end, $\omega\tau_c >> 1$ (low temperature regime) is the slow limit, where τ_c is fairly long.

relaxation rate. As shown in Fig. 6.1, when $\omega\tau_c = 1$, the amount of molecules reorienting at Larmor frequency peaks, and as a result this is the condition where spin-lattice relaxation is most efficient.

6.3 Debye Relaxation

In the presence of an external alternating electric field, Debye relaxation is commonly assumed to describe electric polarization with a single relaxation time, if the system is described as an ensemble of independent paraelectric dipoles with thermally randomized orientations. The model can be derived from a rotational diffusive framework, where the motion of the fluctuating permanent dipoles is driven by stochastic thermal energy, while hindered by an on-site lattice potential. The time dependent characteristic of the polarization of a system

follows the form of a first order differential equation [69, 70, 78]

$$\frac{d\boldsymbol{p}(t)}{dt} = -\frac{1}{\tau}\boldsymbol{p}(t), \tag{6.4}$$

$$\tau = \tau_0 \exp(\frac{\Delta}{k_B T}), \tag{6.5}$$

where τ is the characteristic relaxation time taken to follow a simple thermally activated behavior, with Δ the associated activation barrier for motion. The complex response function can be derived from the above characteristic. The complex response function that results are real part K' and loss tangent $tan\delta$ given as

$$K' = 1 + \chi_b + \frac{\chi_r(0)}{1 + (\omega\tau)^2}, \tag{6.6}$$

$$\tan\delta = \frac{\chi_r(0)(\omega\tau)}{[1 + \chi_r(0) + \chi_b] + (1 + \chi_b)(\omega\tau)^2}, \tag{6.7}$$

where ω is the angular frequency of the applied alternating electric field. $1 + \chi_b$ and $\chi_r(0)$ correspond to the real-part high ($\omega\tau < 1$) and low frequency ($\omega\tau > 1$) extrapolations, respectively. $1 + \chi_b$ is assocaited with vacuum permitivity and the background contribution from the material; whereas, $\chi_r(0)$ is corresponding to the response when the underlying dynamics is faster than measurement frequency. Loss peaks are expected when the condition $\omega\tau = 1$ is met.

The dielectric measurements were carried out with a capacitance bridge method, configured for 3-terminal measurements. The measurements were made at three audio frequencies, 300 Hz, 1 kHz, and 10 kHz on a powder sample. The home-made capacitor setup was thermally anchored to a cold finger on a closed cycle cryostat, for measurements covering the range 20 - 270 K.

6.3.0.1 Alternative Debye Analysis for the Rotor Dynamics

The principle of dielectric measurement applies only to system with permanent dipoles. The real part $\epsilon^{'}$ and the imaginary part $\epsilon^{''}$ of the dielectric constant can be expressed as

$$\epsilon^{'} = \epsilon_{\infty} + \frac{\epsilon_s - \epsilon_{\infty}}{1 + \omega^2\tau^2}, \tag{6.8}$$

$$\epsilon^{''} = \frac{\epsilon_s - \epsilon_{\infty}}{1 + \omega^2\tau^2}, \tag{6.9}$$

where ϵ_{∞} is the permittivity in the high frequency limit, ϵ_s, the static permittivity, is the zero frequency dielectric permittivity. τ is the correlation time of the molecules. Technically, for a perfect capacitor with crystalline molecular rotors as the dielectric material, the motion of the rotating molecules would be the exclusive contribution to the dielectric loss, which is modelled as

$$\tan(\delta) = \frac{C_R}{C_0}\frac{\omega\tau}{1 + \omega^2\tau^2}, \tag{6.10}$$

where ω is the measurement angular frequency. C_0 is comprised of capacitance resulting from electrode capacitance and the framework part of the crystalline molecular rotors, which is normally on the order of 1 pF. In an ideal case of parallel plate capacitor with cross sectional area L^2 and a gap L where the material of crystalline dipolar molecular motors is homogeneously filled, C_R is given by

$$C_R = \frac{\epsilon_R + 2}{3}\frac{Np_0^2}{3k_BTL^2}(\cosh(\frac{S}{2k_BT}))^{-2}. \tag{6.11}$$

The above two equations along with Arrhenius equation can be exploited to simulate (or predict) the location $\omega\tau = 1$ where a loss peak would occur, which is governed by both temperature and probing frequency. The magnitude of the loss peak is contingent on the strength of each dipole moment p_0 and total quantity of rotating molecules in the sample measured. Treating the rotors in the dilute limit amounts to a local field correction $\frac{\epsilon+2}{3}$. The local field correction factor $\frac{\epsilon+2}{3}$ [70] is on the order of unity so would not significantly affect the resultant simulated dielectric loss. The $(\cosh(\frac{S}{2k_BT}))^{-2}$ factor takes into account, due to decrease in temperature, firstly the decrease in signal and secondly the increase in the

population of rotors in a preferential direction [69–71, 79]. Namely, the hyperbolic cosine factor serves to suppress the dielectric loss signal as the decrease in temperature leads to the population of dipole moments evidently prefer potential wells of certain directions, due to correlation effects (in our case antiferroelectric) amid the dipoles. S is the asymmetrical energy scale that accounts for the preference. This alternative way of approaching the Debye dynamic crossover could qualitatively account for the difference in loss peak height.

Bibliography

[1] T M Rice and M Sigrist. Sr2RuO4: an electronic analogue of 3He ? Journal of Physics: Condensed Matter, 7(47):L643–L648, 1995.

[2] Andrew Peter Mackenzie and Yoshiteru Maeno. The superconductivity of Sr2RuO4 and the physics of spin-triplet pairing. Reviews of Modern Physics, 75(2):657–712, 2003.

[3] C. W. Hicks, D. O. Brodsky, E. A. Yelland, A. S. Gibbs, J. A. N. Bruin, M. E. Barber, S. D. Edkins, K. Nishimura, S. Yonezawa, Y. Maeno, and A. P. Mackenzie. Strong increase of Tc of Sr2RuO4 under both tensile and compressive strain. Science, 344(6181):283–285, 2014.

[4] Alexander Steppke, Lishan Zhao, Mark E. Barber, Thomas Scaffidi, Fabian Jerzembeck, Helge Rosner, Alexandra S. Gibbs, Yoshiteru Maeno, Steven H. Simon, Andrew P. Mackenzie, and Clifford W. Hicks. Strong peak intc of Sr2RuO4 under uniaxial pressure. Science, 355(6321):eaaf9398, 2017.

[5] K. Ishida, H. Mukuda, Y. Kitaoka, K. Asayama, Z. Q. Mao, Y. Mori, and Y. Maeno. Spin-triplet superconductivity in Sr2RuO4 identified by 17O knight shift. Nature, 396(6712):658–660, 1998.

[6] Cortnie S. Vogelsberg and Miguel A. Garcia-Garibay. Crystalline molecular machines: function, phase order, dimensionality, and composition. Chem. Soc. Rev., 41(5):1892–1910, 2012.

[7] James Keeler. Understanding NMR Spectroscopy. 2010.

[8] P. Krantz, M. Kjaergaard, F. Yan, T. P. Orlando, S. Gustavsson, and W. D. Oliver. A quantum engineer's guide to superconducting qubits. Applied Physics Reviews, 6(2):021318, 2019.

[9] https://www.nobelprize.org/.

[10] J. D. Badjic. A molecular elevator. Science, 303(5665):1845–1849, 2004.

[11] Abbott. Quantum Aspects of Life. Imperial College Press, 2008.

[12] R. Dean Astumian. Thermodynamics and kinetics of a brownian motor. Science, 276(5314):917–922, 1997.

[13] J. Vacek and J. Michl. Molecular dynamics of a grid-mounted molecular dipolar rotor in a rotating electric field. Proc. Natl. Acad. Sci. U.S.A., 98(10):5481–5486, 2001.

[14] Gregg S. Kottas, Laura I. Clarke, Dominik Horinek, and Josef Michl. Artificial molecular rotors. Chem. Rev., 105(4):1281–1376, 2005.

[15] Robert D. Horansky, Laura I. Clarke, John C. Price, Tinh-Alfredo V. Khuong, Peter D. Jarowski, and Miguel A. Garcia-Garibay. Dielectric response of a dipolar molecular rotor crystal. Phys. Rev. B, 72(1), 2005.

[16] Hung Dang Carlos N. Sanrame Jose E. Nuñez Zaira Dominguez, Tinh-A. V. Khuong and Miguel A. Garcia-Garibay. Molecular compasses and gyroscopes with polar rotors: Synthesis and characterization of crystalline forms. J. Am. Chem. Soc., 125(29):8827–8837, 2003.

[17] M. A. Garcia-Garibay. Crystalline molecular machines: Encoding supramolecular dynamics into molecular structure. Proc. Natl. Acad. Sci. U.S.A., 102(31):10771–10776, 2005.

[18] Carlos E. Godinez, Gerardo Zepeda, and Miguel A. Garcia-Garibay. Molecular compasses and gyroscopes. II. synthesis and characterization of molecular rotors with axially substituted bis[2-(9-triptycyl)ethynyl]arenes. Journal of the American Chemical Society, 124(17):4701–4707, 2002.

[19] Carlos E. Godinez, Gerardo Zepeda, Christopher J. Mortko, Hung Dang, and Miguel A. Garcia-Garibay. Molecular crystals with moving parts: Synthesis, characterization, and

crystal packing of molecular gyroscopes with methyl-substituted triptycyl frames. The Journal of Organic Chemistry, 69(5):1652–1662, 2004.

[20] Miguel A. Garcia-Garibay and Carlos E. Godinez. Engineering crystal packing and internal dynamics in molecular gyroscopes by refining their components. fast exchange of a phenylene rotator by 2H NMR. Crystal Growth & Design, 9(7):3124–3128, 2009.

[21] Keith J. Laidler. Reaction Kinetics: Homogeneous Gas Reactions. Pergamon, 2013.

[22] R. E. Weston and H. A. Schwarz. Chemical Kinetics. Prentice-Hall, Inc., Englewood Cliffs, New Jersey,, 1972.

[23] Carlos E. Godinez Tinh-Alfredo V. Khuong, Jose E. Nuñez and Miguel A. Garcia-Garibay. Crystalline molecular machines: A quest toward solid-state dynamics and function. Acc. Chem. Res., 39(6):413–422, 2006.

[24] Ryogo Kubo and Kazuhisa Tomita. A general theory of magnetic resonance absorption. Journal of the Physical Society of Japan, 9(6):888–919, 1954.

[25] A.G. Redfield. The theory of relaxation processes. In Advances in Magnetic Resonance, pages 1–32. Elsevier, 1965.

[26] N. E. Hussey, A. P. Mackenzie, J. R. Cooper, Y. Maeno, S. Nishizaki, and T. Fujita. Normal-state magnetoresistance of Sr2RuO4. Physical Review B, 57(9):5505–5511, 1998.

[27] T. Katsufuji, M. Kasai, and Y. Tokura. In-plane and out-of-plane optical spectra of Sr2RuO4. Physical Review Letters, 76(1):126–129, 1996.

[28] Yoshiteru Maen Toshizo Fujita Stephen R. Julian Andrew P. Mackenzie, Shin-ichi Ikeda and Gilbert G. Lonzarich. The fermi surface topography of Sr2RuO4. Journal of the Physical Society of Japan, 67(2):385–388, 1998.

[29] A. P. Mackenzie, S. R. Julian, A. J. Diver, G. J. McMullan, M. P. Ray, G. G. Lonzarich, Y. Maeno, S. Nishizaki, and T. Fujita. Quantum oscillations in the layered perovskite superconductor Sr2RuO4. Physical Review Letters, 76(20):3786–3789, 1996.

[30] Hiroaki Hashimoto Shuji Nishizaki Shin-ichi Ikeda Minoru Nohara Toshizo Fujita Andrew P. Mackenzie NigelE. Hussey J. Georg Bednorz Yoshiteru Maeno, Koji Yoshida and Frank Lichtenberg. Two-dimensional fermi liquid behavior of the superconductor Sr2RuO4. Journal of the Physical Society of Japan, 66(5):1405–1408, 1997.

[31] Tamio Oguchi. Electronic band structure of the superconductor Sr2RuO4. Physical Review B, 51(2):1385–1388, 1995.

[32] Y. Maeno, K. Yoshida H. Hashimoto, T. Fujita S. Nishizaki, J. G. Bednorz, and F. Lichtenberg. Superconductivity in a layered perovskite without copper. Nature, 372(6506):532–534, 1994.

[33] G. M. Luke, Y. Fudamoto, K. M. Kojima, M. I. Larkin, J. Merrin, B. Nachumi, Y. J. Uemura, Y. Maeno, Z. Q. Mao, Y. Mori, H. Nakamura, and M. Sigrist. Time-reversal symmetry-breaking superconductivity in Sr2RuO4. Nature, 394(6693):558–561, 1998.

[34] Jing Xia, Yoshiteru Maeno, Peter T. Beyersdorf, M. M. Fejer, and Aharon Kapitulnik. High resolution polar kerr effect measurements Sr2RuO4: Evidence for broken time-reversal symmetry in the superconducting state. Physical Review Letters, 97(16), 2006.

[35] Anthony J. Leggett. A theoretical description of the new phases of liquid He 3. Reviews of Modern Physics, 47(2):331–414, 1975.

[36] Shingo Yonezawa, Tomohiro Kajikawa, and Yoshiteru Maeno. First-order superconducting transition of Sr2RuO4. Physical Review Letters, 110(7), 2013.

[37] H. Taniguchi S. René de Cotret G. Grissonnanche M.S. Anwar Y. Maeno N. Doiron-Leyraud E. Hassinger, P. Bourgeois-Hope and Louis Taillefer. Vertical line nodes in the superconducting gap structure of Sr2RuO4. Physical Review X, 7(1), 2017.

[38] Shunichiro Kittaka, Shota Nakamura, Toshiro Sakakibara, Naoki Kikugawa, Taichi Terashima, Shinya Uji, Dmitry A. Sokolov, Andrew P. Mackenzie, Koki Irie, Yasumasa Tsutsumi, Katsuhiro Suzuki, and Kazushige Machida. Searching for gap zeros in Sr2RuO4 via field-angle-dependent specific-heat measurement. Journal of the Physical Society of Japan, 87(9):093703, 2018.

[39] Per G. Björnsson, Yoshiteru Maeno, Martin E. Huber, and Kathryn A. Moler. Scanning magnetic imaging of Sr2RuO4. Physical Review B, 72(1), 2005.

[40] Clifford W. Hicks, John R. Kirtley, Thomas M. Lippman, Nicholas C. Koshnick, Martin E. Huber, Yoshiteru Maeno, William M. Yuhasz, M. Brian Maple, and Kathryn A. Moler. Limits on superconductivity-related magnetization in Sr2RuO4 and PrOs4Sb12 from scanning SQUID microscopy. Physical Review B, 81(21), 2010.

[41] Christopher A. Watson, Alexandra S. Gibbs, Andrew P. Mackenzie, Clifford W. Hicks, and Kathryn A. Moler. Micron-scale measurements of low anisotropic strain response of local Tc in Sr2RuO4. Physical Review B, 98(9), 2018.

[42] Igor Marković Mark E. Barber Dijana Milosavljević Federico Mazzola Dmitry A. Sokolov Naoki Kikugawa-Cephise Cacho Pavel Dudin Helge Rosner Clifford W. Hicks Philip D. C. King & Andrew P. Mackenzie Veronika Sunko, Edgar Abarca Morales. Direct observation of a uniaxial stress-driven Lifshitz transition in Sr2RuO4. npj Quantum Materials, 4(1), 2019.

[43] P. Guzman A.P. Dioguardi S.M. Thomas F. Ronning N. Kikugawa D.A. Sokolov F. Jerzembeck A.P. Mackenzie C.W. Hicks E.D. Bauer I.I. Mazin Yongkang Luo, A. Pustogow and S.E. Brown. Normal state O17 NMR studies of Sr2RuO4 under uniaxial stress. Physical Review X, 9(2), 2019.

[44] Henri Alloul. Introduction to the Physics of Electrons in Solids. Springer Berlin Heidelberg, 2011.

[45] Charles P. Slichter. Principles of Magnetic Resonance. Springer Berlin Heidelberg, 1990.

[46] Eiichi Fukushima and Stephen B.W. Roeder. Experimental Pulse NMR. CRC Press, 2018.

[47] A. Abragam. The Principles of Nuclear Magnetism. Oxford University Press, 1983.

[48] I. Pócsik I. Bakonyi, I. Kovács. On the field-dependent broadening of NMR lines in paramagnets. physica status solidi (b), 114(2):609–614, 1982.

[49] H. Alloul. NMR in strongly correlated materials. Scholarpedia, 10(1):30632, 2015. revision #147845.

[50] N. Bloembergen, E. M. Purcell, and R. V. Pound. Relaxation effects in nuclear magnetic resonance absorption. Phys. Rev., 73:679–712, 1948.

[51] V. M. Rozenbaum. Long-range orientational order in a two-dimensional degenerate system of dipoles on a square lattice. JETP Lett., 63(8):662–667, 1996.

[52] D.J. Adams. Calculating the low temperature vapour line by Monte Carlo. Molecular Physics, 32(3):647–657, 1976.

[53] S. W. DeLeeuw, D. Solvaeson, Mark A. Ratner, and Josef Michl. Molecular dipole chains: Excitations and dissipation. J. Phys. Chem. B, 102:3876–3885, 1998.

[54] Eunji Sim, Mark A. Ratner, and Simon W. de Leeuw. Molecular dipole chains II. J. Phys. Chem. B, 103(41):8663–8670, 1999.

[55] J. J. de Jonge, M. A. Ratner, S. W. de Leeuw, and R. O. Simonis. Molecular dipole chains iii: Energy transfer. J. Phys. Chem. B, 108(8):2666–2675, 2004.

[56] J. Vacek and J. Michl. Artificial surface-mounted molecular rotors: Molecular dynamics simulations. Adv. Funct. Mater., 17(5):730–739, 2007.

[57] Jan Neumann, Kay E. Gottschalk, and R. Dean Astumian. Driving and controlling molecular surface rotors with a terahertz electric field. ACS Nano, 6(6):5242–5248, 2012.

[58] Morgan E. Howe and Miguel A. Garcia-Garibay. The roles of intrinsic barriers and crystal fluidity in determining the dynamics of crystalline molecular rotors and molecular machines. J. Org. Chem., 2019.

[59] Takanori Shima, Frank Hampel, and J. A. Gladysz. Molecular gyroscopes: Fe(CO)3 and Fe(CO)2(NO)+ rotators encased in three-spoke stators; facile assembly by alkene metatheses†. Angew. Chem. Int. Ed., 43(41):5537–5540, 2004.

[60] Tomoyuki Akutagawa, Hiroyuki Koshinaka, Daisuke Sato, Sadamu Takeda, Shin-Ichiro Noro, Hiroyuki Takahashi, Reiji Kumai, Yoshinori Tokura, and Takayoshi Nakamura. Ferroelectricity and polarity control in solid-state flip-flop supramolecular rotators. Nat. Mater., 8(4):342–347, 2009.

[61] Wataru Setaka and Kentaro Yamaguchi. A molecular balloon: Expansion of a molecular gyrotop cage due to rotation of the phenylene rotor. J. Am. Chem. Soc., 134(30):12458–12461, 2012.

[62] Wataru Setaka and Kentaro Yamaguchi. Order-disorder transition of dipolar rotor in a crystalline molecular gyrotop and its optical change. J. Am. Chem. Soc., 135(39):14560–14563, 2013.

[63] Angiolina Comotti, Silvia Bracco, Atsushi Yamamoto, Mario Beretta, Tomofumi Hirukawa, Norimitsu Tohnai, Mikiji Miyata, and Piero Sozzani. Engineering switchable rotors in molecular crystals with open porosity. J. Am. Chem. Soc., 136(2):618–621, 2014.

[64] Zi-Shuo Yao, Kaoru Yamamoto, Hong-Ling Cai, Kazuyuki Takahashi, and Osamu Sato. Above room temperature organic ferroelectrics: Diprotonated 1,4-diazabicyclo[2.2.2]octane shifts between two 2-chlorobenzoates. J. Am. Chem. Soc., 138(37):12005–12008, 2016.

[65] Silvia Bracco, Fabio Castiglioni, Angiolina Comotti, Simona Galli, Mattia Negroni, Angelo Maspero, and Piero Sozzani. Ultrafast molecular rotors and their CO2 tuning

in MOFs with rod-like ligands. Chemistry - A European Journal, 23(47):11210–11215, 2017.

[66] Cortnie S. Vogelsberg, Fernando J. Uribe-Romo, Andrew S. Lipton, Song Yang, K. N. Houk, Stuart Brown, and Miguel A. Garcia-Garibay. Ultrafast rotation in an amphidynamic crystalline metal organic framework. Proc. Natl. Acad. Sci. U.S.A., 114(52):13613–13618, 2017.

[67] C.J.F.Böttcher. Theory of Electric Polarization, volume 1. Elsevier, 2 edition, 1973.

[68] M.J. et al Frisch. Gaussian09. Technical report, Gaussian, Inc., Wallingford, CT, 2013.

[69] P. Debye. Polar molecules. Journal of the Society of Chemical Industry, 48(43):1036–1037, 1929.

[70] Frohlich. Theory of Dielectrics: Dielectric Constant and Dielectric Loss. Oxford University Press, 1987.

[71] Friedrich Kremer and Andreas Schönhals, editors. Broadband Dielectric Spectroscopy. Springer Berlin Heidelberg, 2003.

[72] Yan Zhao and Donald G. Truhlar. The M06 suite of density functionals for main group thermochemistry, thermochemical kinetics, noncovalent interactions, excited states, and transition elements: two new functionals and systematic testing of four M06-class functionals and 12 other functionals. Theor. Chem. Acc., 120(1-3):215–241, 2007.

[73] Jacques Kotze. Introduction to Monte Carlo methods for an ising model of a ferromagnet. arXiv:0803.0217, 2008.

[74] Hisao Nakanishi Nicholas J. Giordano. Computational Physics. Pearson; 2 edition, 2005.

[75] William B. Heard W. B. Heard. Rigid Body Mechanics. Wiley VCH Verlag GmbH, 2005.

[76] Horacio A. Farach. Magnetic Resonance of Phase Transitions. Academic Press, 1979.

[77] Kurt Binder and Dieter W. Heermann. Monte Carlo Simulation in Statistical Physics. Springer International Publishing, 2019.

[78] C. J. F. Bottcher and P. Bordewijk. Theory of Electric Polarization Vol2 Dielectrics in Time Dependent Fields. Elsevier Science, 1980.

[79] Robert D. Horansky, Laura I. Clarke, Erick B. Winston, John C. Price, Steven D. Karlen, Peter D. Jarowski, Rosa Santillan, and Miguel A. Garcia-Garibay. Dipolar rotor-rotor interactions in a difluorobenzene molecular rotor crystal. Phys. Rev. B, 74(5), 2006.